https://doi.org/10.5194/egusphere-2026-4728
Preprint. Discussion started: 8 September 2026
© Author(s) 2026. CC BY 4.0 License.

The Lozano Closure: A TOA-Normalised Spectral Mapping Between Broadband Shortwave Radiation and PAR

Ismael López Lozano[1], Ekaterina Ezhova[1], Inamculada Foyo-Moreno[2,3], Inmaculada Alados[3,4], Markku Kulmala[1]

[1]Institute for Atmospheric and Earth System Research, University of Helsinki, Helsinki, 00014, Finland
[2]Department of Applied Physic, University of Granada, Granada, 18071, Spain
[3]Andalusian Institute for Earth System Research, Granada, 18006, Spain
[4]Department of Applied Physics II, University of Málaga, Málaga, 29071, Spain

Correspondence to: Ismael L. Lozano (ismael.lozano@helsinki.fi)

Abstract. Accurate reconstruction of photosynthetically active radiation (PAR) from broadband shortwave (SW) measurements remains central to biosphere–atmosphere studies and ecosystem modelling. Most existing approaches rely on empirical regressions, machine-learning techniques, or site-specific calibration, often treating global and diffuse PAR separately. Here, we introduce the Lozano Closure, a physically constrained transmissivity framework that links broadband shortwave radiation and PAR through a top-of-atmosphere (TOA)-normalised spectral mapping.

The formulation expresses global PAR transmissivity as a power-law function of broadband transmissivity via a spectral exponent α, and diffuse PAR through an additional partition exponent β. Both exponents are derived from log–log transmissivity relations rather than fitted directly to PAR. Across multiple climatic regimes, the non-trivial solution yields pooled $r^2 \approx 0.98$ - 0.99 for global PAR and 0.92 - 0.98 for diffuse PAR without site-specific calibration or auxiliary meteorological inputs.

The exponent α exhibits quasi-stationary behaviour consistent with its interpretation as a band-integrated optical-depth ratio, whereas β reflects the greater regime sensitivity of diffuse partitioning. Sensitivity analysis demonstrates that α depends structurally on the adopted extraterrestrial spectral normalisation, highlighting the importance of coherent TOA definitions for universal implementation.

The Lozano Closure provides a minimal, spectrally consistent alternative to empirical and machine-learning approaches, achieving competitive performance while maintaining cross-site transferability and physical interpretability. The framework is extensible to other spectral bands and offers a pathway toward spectrally coherent sub-band reconstruction within broadband radiation models.

https://doi.org/10.5194/egusphere-2026-4728
Preprint. Discussion started: 8 September 2026
© Author(s) 2026. CC BY 4.0 License.

1 Introduction

Photosynthetically active radiation (PAR, 400–700 nm) represents the spectral portion of solar radiation that drives terrestrial photosynthesis and therefore plays a central role in land–atmosphere carbon exchange. Variations in both global and diffuse PAR directly influence gross primary production, ecosystem carbon uptake, and feedbacks within the climate system (Gu et al., 2002; Mercado et al., 2009). Changes in cloud cover, aerosol loading, and atmospheric composition alter not only the magnitude of incoming solar radiation but also its spectral distribution and diffuse fraction, thereby modulating ecosystem productivity and climate–biosphere interactions (Barnes et al., 2023; Wild, 2012, 2016).

Because atmospheric attenuation is wavelength dependent, perturbations in aerosol optical depth and cloud optical properties do not affect all spectral bands uniformly. Multi-model assessments of effective radiative forcing demonstrate the importance of spectrally resolved aerosol–radiation interactions (Myhre et al., 2013; Thornhill et al., 2020). Recent satellite-based polarimetric retrievals further highlight the role of aerosol absorption in modulating shortwave radiative forcing (Chen et al., 2022). Observational evidence of global dimming and brightening, including clear-sky components, underscores the variability of surface radiation and its climatic relevance (Wild et al., 2021, 2026). Within this context, the PAR spectral interval is particularly sensitive to changes in aerosol optical properties (Lozano et al., 2021).

Despite its importance, direct measurements of PAR - and particularly of its diffuse component - remain substantially less widespread than broadband shortwave observations. While global shortwave radiation is routinely monitored across meteorological networks and long-term research infrastructures (Baldocchi et al., 2001; Nemitz et al., 2018; Pastorello et al., 2020), diffuse PAR observations are comparatively scarce and often temporally limited. This imbalance constrains flux tower analyses, ecosystem modelling, and the evaluation of satellite-derived PAR products.

To address measurement gaps, numerous modelling approaches have been developed to estimate PAR and its diffuse fraction from broadband radiative quantities. Classical parameterisations express diffuse fraction as a function of clearness index (kt) (Erbs et al., 1982; Reindl et al., 1990), and similar kt-based strategies have been extended to PAR using linear, polynomial, or semi-empirical relationships (Foyo-Moreno et al., 2017, 2018; García-Rodríguez et al., 2021, 2022; Lozano et al., 2023). These studies demonstrate that broadband shortwave transmissivity contains substantial information about the radiative processes governing PAR variability.

However, most existing formulations are designed for predictive performance rather than derived from explicit physical constraints linking spectral and broadband attenuation. Empirical regressions often rely on site-dependent coefficients or functional forms selected heuristically, which may limit structural portability across climatic regimes. For applications in process-based land surface models and Earth system models, radiative inputs ideally preserve physical consistency across spectral bands and maintain interpretability under changing atmospheric conditions (Bonan, 2019; Lawrence et al., 2019).

The recurring success of clearness-index-based models suggests that atmospheric transmissivity acts as a dominant low-dimensional control variable linking broadband and spectral radiation components. Yet a formal closure expressing this relationship in a physically constrained and scale-invariant manner has not been established. Such a closure would provide a

https://doi.org/10.5194/egusphere-2026-4728
Preprint. Discussion started: 8 September 2026
© Author(s) 2026. CC BY 4.0 License.

structurally consistent bridge between broadband shortwave transmissivity and PAR, enabling estimation of both global and diffuse components without site-specific calibration.

In this study, we develop the Lozano Closure (LC), a physically based, top-of-atmosphere-normalised framework linking broadband shortwave transmissivity to both global and diffuse PAR. The closure is derived from band-integrated radiative principles and validated across multiple measurement sites spanning diverse climatic regimes. By relying exclusively on broadband shortwave radiative quantities and preserving transmissivity structure, the proposed formulation provides a physically interpretable alternative to empirical regressions while remaining suitable for applications requiring spatial scalability and structural consistency.

2 Conceptual framework and theoretical basis

2.1 Spectral dependence of atmospheric attenuation

Solar radiation reaching the Earth's surface is attenuated by absorption and scattering due to atmospheric gases, aerosols, and clouds. These processes are intrinsically wavelength-dependent and are commonly described in terms of spectral optical depth and slant path geometry (Bohren, 2006; Iqbal, 1983; Stamnes et al., 2017). For monochromatic radiation, attenuation along a slanted atmospheric path of zenith angle θ follows the Beer–Lambert law,

$$I_\lambda = I_{0,\lambda} e^{-\tau_\lambda m} \quad , \qquad (1)$$

where $I_{0,\lambda}$ is the extraterrestrial spectral irradiance, τ_λ is the optical depth, and $m \approx \sec\theta$ is the relative optical air mass. Optical depth represents the vertically integrated extinction coefficient and quantifies the cumulative attenuation experienced by radiation propagating through the atmosphere. In the real atmosphere, extinction arises from multiple components, molecular absorption, Rayleigh scattering, aerosol scattering and absorption, and cloud extinction, whose optical depths add in τ-space (Emery and Camps, 2017),

$$\tau_\lambda = \tau_\lambda^{gas} + \tau_\lambda^{aer} + \tau_\lambda^{cloud} + \cdots \; . \qquad (2)$$

Because optical depths combine additively while transmissivities multiply, atmospheric attenuation exhibits a fundamentally multiplicative structure in transmissivity space.

When integrated over a spectral interval, these wavelength-dependent processes yield band-integrated irradiances. The photosynthetically active radiation (PAR, 400–700 nm) and broadband shortwave radiation (SW, typically 300 - 3000 nm) originate from the same extraterrestrial solar spectrum but differ in spectral weighting. Since both the solar spectral distribution and atmospheric extinction efficiencies vary with wavelength, the effective attenuation experienced by PAR need not mirror that of SW.

Diffuse radiation is particularly sensitive to these spectral effects. Cloud droplets and aerosol particles modify both the angular distribution and spectral composition of transmitted radiation. As a result, both global and diffuse PAR are governed by the same atmospheric processes that control SW radiation, but potentially with different effective spectral responses.

https://doi.org/10.5194/egusphere-2026-4728
Preprint. Discussion started: 8 September 2026
© Author(s) 2026. CC BY 4.0 License.

2.2 Broadband transmissivity as a low-dimensional atmospheric descriptor

In practice, surface radiation measurements are available as band-integrated quantities rather than spectrally resolved fluxes. A convenient dimensionless descriptor of broadband atmospheric transmission is the clearness index,

$$k_{t,SW} = \frac{I_{SW}}{I_{0,SW}} \quad , \tag{3}$$

where I_{SW} is the surface global horizontal shortwave irradiance and $I_{0,SW}$ is the corresponding extraterrestrial horizontal irradiance. The clearness index represents the fraction of top-of-atmosphere shortwave radiation transmitted to the surface after accounting for atmospheric attenuation and solar geometry. Similarly, the broadband diffuse fraction is defined as

$$k_{d,SW} = \frac{I_{SW,d}}{I_{SW}} \quad , \tag{4}$$

where $I_{SW,d}$ is the diffuse component of shortwave radiation. Together, $k_{t,SW}$ and $k_{d,SW}$ provide compact, dimensionless measures of total transmission and diffuse partitioning.

Although these indices are broadband quantities, extensive empirical evidence shows that geometrically normalised surface irradiance collapses onto well-defined, monotonic relationships with clearness index across a wide range of atmospheric conditions. Classical diffuse fraction parameterisations (e.g., Erbs et al., 1982; Reindl et al., 1990) exploit this behaviour, expressing diffuse fraction as a function of clearness index. Similar regularities have been documented for PAR. Empirical studies demonstrate that both global and diffuse PAR respond systematically to variations in broadband shortwave transmissivity across diverse sky regimes (Foyo-Moreno et al., 2017, 2018; Lozano et al., 2022, 2023).

These results indicate that much of the physically relevant variability in PAR is already encoded in broadband shortwave transmissivity. After geometric normalisation, both SW and PAR behave as low-dimensional functions of atmospheric transmission.

The multiplicative structure implied by optical depth formulations further suggests that structured and bounded mappings should exist between broadband transmittances in different spectral intervals. If extinction processes combine additively in optical depth space and multiplicatively in transmissivity space, then band-integrated responses across spectral ranges may be expressible through scale-consistent transformations of broadband transmittance rather than through arbitrary regression functions. The conceptual relationship between extraterrestrial radiation, spectral attenuation, broadband transmissivity, and surface PAR is illustrated schematically in Figure 1.

The monotonic collapse of geometrically normalised irradiance onto clearness index suggests that atmospheric attenuation behaves predominantly as a transmissivity-driven process. This observation motivates the formulation of a physically constrained closure linking SW transmissivity and PAR transmittance. The objective is to derive a minimal, scale-consistent relationship grounded in the multiplicative structure of atmospheric extinction. The formal development of this closure, and its admissible solutions, are presented in Section 5.

https://doi.org/10.5194/egusphere-2026-4728
Preprint. Discussion started: 8 September 2026
© Author(s) 2026. CC BY 4.0 License.

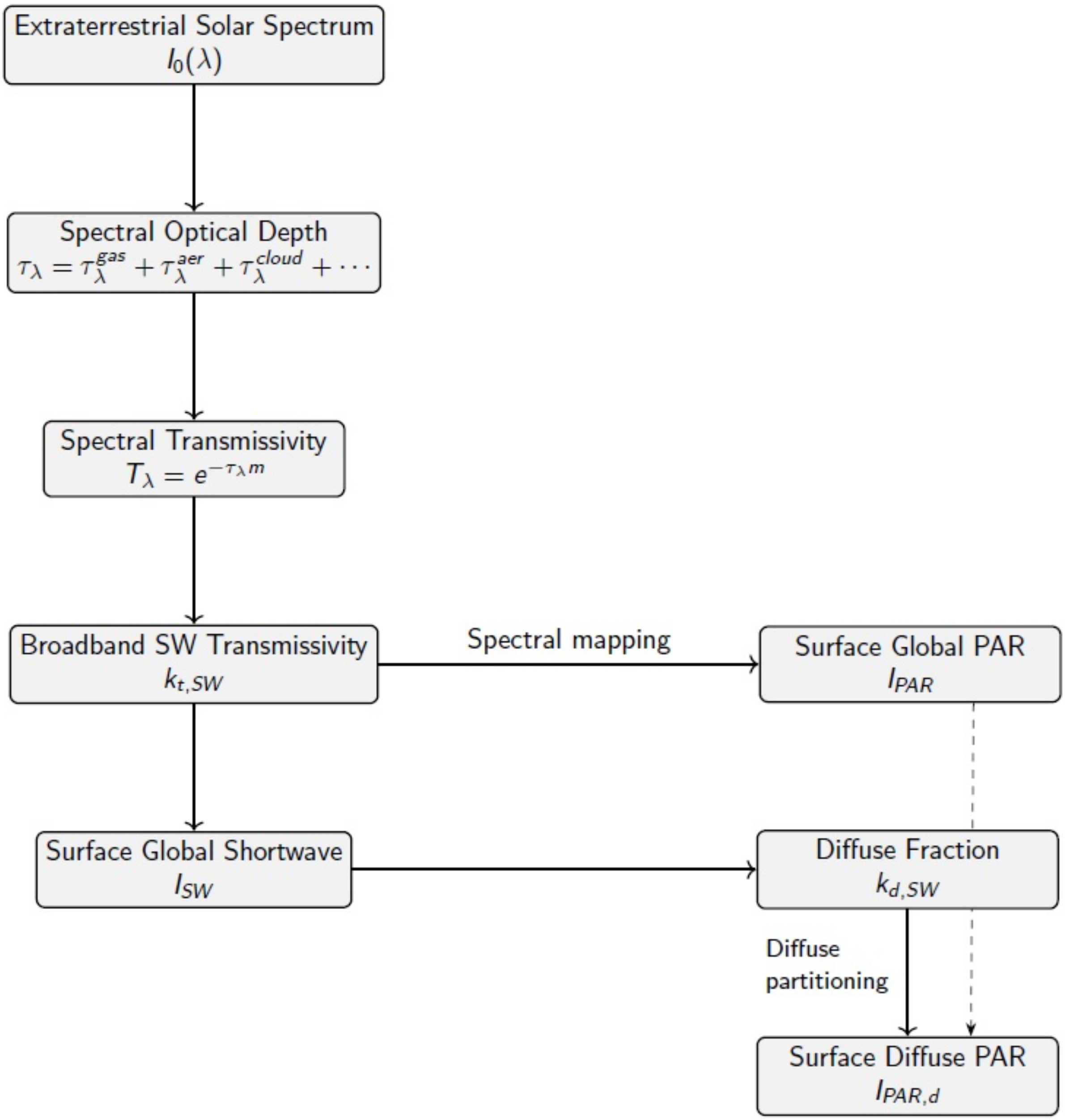

Figure 1: Conceptual representation of the relationship between extraterrestrial solar radiation, spectral atmospheric attenuation, broadband shortwave transmissivity (k_t), and the resulting surface PAR response. Broadband transmissivity integrates the dominant atmospheric attenuation processes, which also govern PAR through spectral weighting.

https://doi.org/10.5194/egusphere-2026-4728
Preprint. Discussion started: 8 September 2026
© Author(s) 2026. CC BY 4.0 License.

3 Data and study sites

3.1 Measurement sites

To evaluate the structural validity and climatic robustness of the LC, we employed long-term surface radiation measurements from Southern Europe (Spain) and multiple ICOS ecosystem stations spanning Central and Northern Europe (Figure 2). The selected sites cover contrasting latitudes, elevations, and ecosystem types. This multisite and multiyear coverage of the datasets ensures representation of seasonal variability and a wide range of solar zenith angles (θ) and a broad variability in atmospheric conditions including cloud regimes. The dataset includes high-quality measurements of global and diffuse radiation for both SW and PAR from two Spanish stations and five ICOS Class 1 stations. A summary of the measurement sites, including locations, coordinates, elevations, data periods, ecosystem types, climates, and references to the dataset is provided in Table 1.

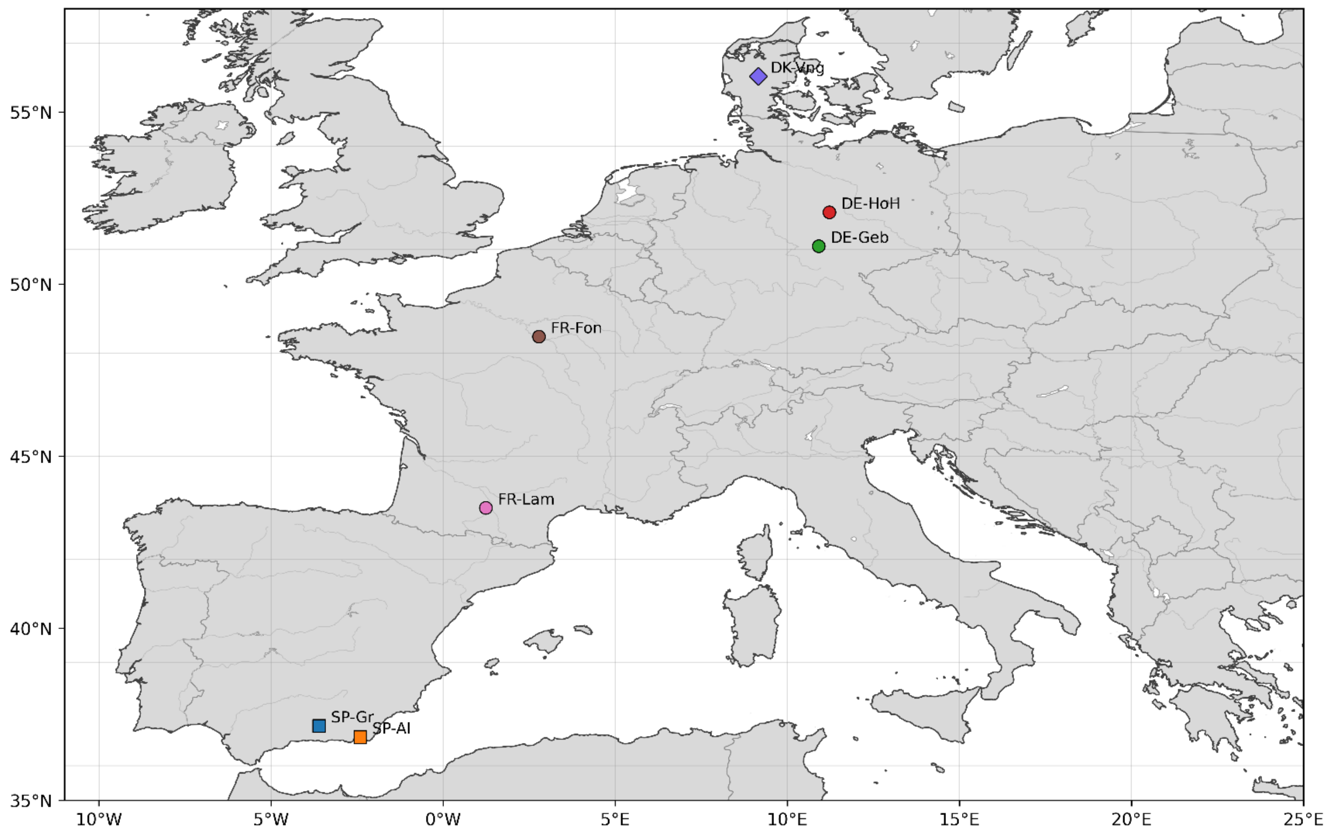

Figure 2: Geographic location of the measurement sites used in this study. Spanish radiometric stations (Granada and Almería) and ICOS ecosystem sites across Germany, Denmark, and France are shown. Coordinates are indicated in a Plate Carrée projection.

The Mediterranean sites (Spanish stations) are located in Granada (ES-Gr, 37.16°N, 3.61°W; 680 m a.s.l.; years 1994 - 1995) and Almería (ES-Al, 36.83°N, 2.41°W; 21 m a.s.l.; years 1993 - 1995), these datasets have been employed previously in manuscript related to PAR modelling (e.g., Alados et al., 2002; Foyo-Moreno et al., 2018; Lozano et al., 2023) ensuring the robustness of conclusions drawn from them and their intercomparability with prior work. Granada is situated in a continental Mediterranean climate with strong seasonal variability in climatic and aerosol loads, while the Almería site is coastal, at low elevation, and influenced by marine conditions. In addition to these characteristics, both Spanish stations are influenced by episodic Saharan dust events. For the present study, only the historical datasets from the 1990s were used, as these are the only available periods including simultaneous measurements of both global and diffuse PAR.

For the transect covering Central to Northern Europe, measurements were obtained from five ICOS Class 1 stations. The first station is located in Lamasquère, France (FR-Lam, 43.50°N, 1.24°E; 181 m a.s.l.; years 2020 – 2024; Brut et al., 2025), a cropland in a flat large alluvial valley near Toulouse, with maize-wheat rotation. Its climate corresponds to a marine west coast (Cfb). The second station, also in France, is Fontainebleau-Barbeau (FR-Fon, 48.48°N, 2.78°E; 103 m a.s.l.; years 2019 – 2025; Berveiller et al., 2025), located near Paris, within the Atlantic Biogeographical Region in a deciduous oak forest, with a temperate oceanic climate representative of a large North-Western part of Europe. The next station is located in Gebesee, Germany (DE-Geb, 51.10°N, 10.91°E; 163 m a.s.l., years 2020 – 2025; Brümmer et al., 2025), an agricultural site with crop rotation within a Marine west coast climate zone (Cfb). The fourth station, in Hohes Holz, Germany (DE-Hoh, 48.48°N, 2.78°E; 217 m a.s.l., years 2019 – 2025; Rebmann et al., 2025), is located at the northern border of the Bode water catchment and consists of an alluvial forest of deciduous broadleaf trees. Its climate zone is a Marine west coast (Cfb). The last station is in Voulundgaard, Denmark (DK-Vng, 56.04°N, 9.16°E; 67 m a.s.l., years 2020 – 2023; Friborg et al., 2024), a cropland located in the eastern part of the Skjern River catchment in central Jutland, west of the margin for the ice extent of the last glacial maximum, characterized by flat terrain on sandy soil. This station is part of the HOBE Hydrological Observatory.

Table 1: Summary of measurement sites, including site codes, locations, coordinates, elevations, data periods, ecosystem types, climates, and dataset references.

https://doi.org/10.5194/egusphere-2026-4728
Preprint. Discussion started: 8 September 2026
© Author(s) 2026. CC BY 4.0 License.

Site Code	Location	Latitude (°N)	Longitude (°E/W)	Elevation (m a.s.l.)	Data Years	Ecosystem Type	Climate	Reference
ES-Gr	Granada, Spain	37.16	-3.61	680	1994–1995	Urban	Continental Mediterranean	-
ES-Al	Almería, Spain	36.83	-2.41	21	1993–1995	Urban	Coastal Mediterranean	-
FR-Lam	Lamasquère, France	43.5	1.24	181	2020–2024	Cropland (maize-wheat rotation)	Marine west coast (Cfb)	Brut et al. (2024)
FR-Fon	Fontainebleau-Barbeau, France	48.48	2.78	103	2019–2025	Deciduous oak forest	Temperate oceanic	Berveiller et al. (2025)
DE-Geb	Gebesee, Germany	51.1	10.91	163	2020–2025	Agricultural (crop rotation)	Marine west coast (Cfb)	Brümmer et al. (2025)
DE-HoH	Hohes Holz, Germany	52.09	11.22	217	2019–2025	Alluvial forest (deciduous broadleaf)	Marine west coast (Cfb)	Rebmann et al. (2025)
DK-Vng	Voulundgaard, Denmark	56.04	9.16	67	2020–2023	Cropland	Marine west coast (Cfb)	Friborg et al. (2024)

https://doi.org/10.5194/egusphere-2026-4728
Preprint. Discussion started: 8 September 2026
© Author(s) 2026. CC BY 4.0 License.

3.2 Instrumentation and measurements

At the Spanish sites, Granada and Almería, PAR was measured using Li-Cor LI-190SA quantum sensors (Lincoln, NE, USA), while SW was measured using Kipp & Zonen CM-11 pyranometers (Delft, Netherlands). One instrument of each type was mounted on a polar-axis shadowband system to determine diffuse components. The LI-190SA sensors have a relative error below 5%, while the CM-11 pyranometers exhibit directional errors below 10 W m^{-2} for θ up to 80° (manufacturer specifications). Diffuse measurements were corrected following (Batlles et al., 1995), for more details in the instrument configuration see Lozano et al. (2023). Data were recorded at 1-minute intervals and aggregated to hourly values.

At the ICOS Class 1 sites, SW is measured using CNR4 net radiometers (Kipp & Zonen, Delft, Netherlands) equipped with CNF4 ventilation and heating units, with directional errors below 10 W m^{-2} for θ up to 80° and daily sum accuracy of ±5% (manufacturer specifications). For PAR, PQS1 quantum sensors (Kipp & Zonen) or LI-190R sensors (LI-COR, Lincoln, NE, USA) are employed, with relative errors below 5%. Diffuse radiation is measured using SPN1 or BF5 sensors (Delta-T Devices, Burwell, UK); the BF5, while not fully compliant with ICOS accuracy thresholds (e.g., potential biases up to 8% in diffuse/total ratios), is used for ratio calculations and corrected in post-processing by scaling to compliant sensors like PQS1 or SPN1 to ensure data quality (Carrara et al., 2018). Instrumentation adheres to ICOS standardized protocols, with traceability according to WMO protocols, factory calibrations every 2 years (or as needed for spares), intercomparability ensured through uniform sensor setups and centralized data harmonization at the Ecosystem Thematic Centre (ETC), and quality control involving automatic plausibility checks, alert systems for inconsistencies, and multi-level processing (raw to final validated data) for reproducibility across the network (Carrara et al., 2018). Data are recorded at high frequency and aggregated to half-hourly intervals.

Across all stations, PAR measurements, originally recorded in photon flux density units (µmol m^{-2} s^{-1}), were converted to energy units (Wm^{-2}) using a standard conversion factor of 4.57 µmol J^{-1} (McCree, 1972) to ensure consistency in the dataset.

4 Data processing and quality control

A multi-step quality-control procedure was applied following the approach previously implemented in Lozano et al. (2023) and adapted here for a multi-site framework to ensure physical consistency and cross-site comparability across the ICOS Class 1 and Spanish radiometric datasets. The procedure included unit homogenisation, computation of derived radiative indices, physical plausibility constraints, statistical envelope filtering, and final visual verification.

First, non-physical values were removed. Negative radiation measurements were excluded, and physically constrained indices were enforced such that clearness index and diffuse fraction satisfied $0 < k_t < 1$ and $0 < k_d < 1$. Measurements recorded at θ greater than 80° were discarded in order to minimise cosine-response errors and excessive optical path-length effects under low solar elevations.

To ensure spectral consistency between SW and PAR, additional plausibility bounds were applied to the PAR-to-SW ratio. Values falling outside a broad physically realistic range (approximately 1 - 2.5 µmol J^{-1} under natural atmospheric conditions)

https://doi.org/10.5194/egusphere-2026-4728
Preprint. Discussion started: 8 September 2026
© Author(s) 2026. CC BY 4.0 License.

were removed, as such deviations typically indicate sensor malfunction, shading artefacts, or calibration inconsistencies rather than atmospheric variability.

Residual anomalous values were identified using a percentile-based envelope method adapted to solar radiation data. Cosine of θ was discretised into equal bins spanning the range 0 - 1. Within each bin, the 1st and 99th percentiles of global and diffuse PAR were computed to define physically admissible envelopes. For global PAR, only the upper envelope constraint was applied, as extremely low values are physically plausible under dense cloud conditions, whereas unrealistically high values typically indicate sensor artefacts. For diffuse PAR, both lower and upper envelopes were enforced to remove non-physical partitioning behaviour. Throughout the process, intermediate and final datasets were visually inspected to verify the absence of systematic artefacts, discontinuities, or residual sensor anomalies. The resulting datasets are physically consistent, spectrally coherent, and suitable for evaluating the structural behaviour of the LC across diverse climatic regimes.

5 The Lozano Closure: theoretical formulation and admissible solutions

5.1 Band-integrated surface irradiance

For a given spectral band B = [λ_{min}, λ_{max}], the downwelling surface irradiance, I, can be expressed as the band-integrated extraterrestrial spectral irradiance, $I_0(\lambda)$, weighted by the atmospheric transmittance, $T(\lambda)$,

$$I_B = \int_{\lambda_{min}}^{\lambda_{max}} I_0(\lambda) T(\lambda) d\lambda \,. \quad (5)$$

In practice, surface radiation measurements are available as band-integrated quantities, and the detailed spectral structure of $T(\lambda)$ is not resolved. The formulation above therefore motivates the introduction of effective broadband transmittances, which encapsulate the integrated effects of atmospheric attenuation processes, including absorption and scattering by gases, aerosols, and clouds over a given spectral range (Chandrasekhar, 2013; Gueymard, 2003; Stamnes et al., 2017).

5.2 Effective broadband transmittance

A convenient and physically interpretable approximation for atmospheric transmittance is the Beer–Lambert form, which, under monochromatic conditions, expresses the transmittance $T(\lambda)$ along a slanted atmospheric path as

$$T(\lambda) = e^{-\tau_\lambda m}, \quad (6)$$

Where m is the optical air mass, approximating the relative path length through the atmosphere, and is typically approximated by the sec of θ. τ_λ is the spectral optical depth. This representation is widely used in atmospheric optics to describe attenuation along a slanted atmospheric path (Liou, 2002; Noll et al., 2012). Additionally, τ_λ can be expressed as the sum of independent extinction processes in an optical depth space (τ-space; Equation 2),

Although real atmospheric conditions depart from the strict assumptions of Beer–Lambert theory (e.g., multiple scattering under clouds), it is standard practice in broadband solar radiation studies to adopt an effective exponential representation,

$$k_{t,B} \equiv \frac{I_B}{I_{0,B}} \approx e^{-\tau_B^{eff} m} \,, \quad (7)$$

https://doi.org/10.5194/egusphere-2026-4728
Preprint. Discussion started: 8 September 2026
© Author(s) 2026. CC BY 4.0 License.

Where $k_{t,B}$ is the clearness index in band B, $I_{0,B}$ is the extraterrestrial horizontal irradiance for that band, and τ_B^{eff} is an effective broadband optical depth aggregating extinction processes and radiative redistribution within the band (Barnard and Long, 2004). In this representation, the multiplicative structure of transmissivity in T-space reflects the additive structure of extinction in τ-space.

5.3 Closure between SW and PAR transmissivity

Given two spectral ranges of solar radiation, B = SW and B = PAR, the clearness index $k_t = I/I_0$ is interpreted as an effective broadband transmissivity, consistent with the Beer–Lambert formulation. Their effective broadband transmittances can therefore be written as

$$k_{t,SW} \approx e^{-\tau_{SW}^{eff} m} \ , \tag{8}$$

$$k_{t,PAR} \approx e^{-\tau_{PAR}^{eff} m} \ , \tag{9}$$

both bands are governed by the same underlying extinction mechanisms but differ in spectral weighting (Gueymard, 2003; Lozano et al., 2021; Van Laake and Sanchez-Azofeifa, 2005). Figure 3 illustrates the solar spectral irradiance at the top of the atmosphere (TOA) and at the surface, showing the PAR band as a bounded subset of the broader shortwave spectrum. Since atmospheric attenuation acts across the solar spectrum, the band-integrated extinction within the PAR range is expected to scale systematically with that of the full shortwave interval. However, the spectral distribution of extinction is not uniform, with molecular absorption features becoming increasingly important outside the PAR range, particularly in the near-infrared. This provides the physical basis for introducing an effective mapping between SW and PAR transmittances. We introduce the closure assumption that their effective optical depths are proportional,

$$\tau_{PAR}^{eff} = \alpha \tau_{SW}^{eff} \tag{10}$$

where α > 0 is a dimensionless spectral mapping coefficient. Substituting into the effective Beer–Lambert representation yields

$$k_{t,PAR} \approx e^{-\tau_{PAR}^{eff} m} = e^{-\alpha \tau_{SW}^{eff} m} = \left[e^{-\tau_{SW}^{eff} m}\right]^{\alpha} = \left(k_{t,SW}\right)^{\alpha} , \tag{11}$$

Thus, the power-law mapping between SW and PAR transmissivities arises directly from proportionality of effective optical depths. The exponent α therefore represents the ratio between effective broadband optical depths in the PAR and SW spectral ranges. The trivial solution (α = 1) represents the simplest possible closure, assuming identical effective attenuation in both bands; departures from unity reflect systematic spectral differences in extinction and redistribution processes.

https://doi.org/10.5194/egusphere-2026-4728
Preprint. Discussion started: 8 September 2026
© Author(s) 2026. CC BY 4.0 License.

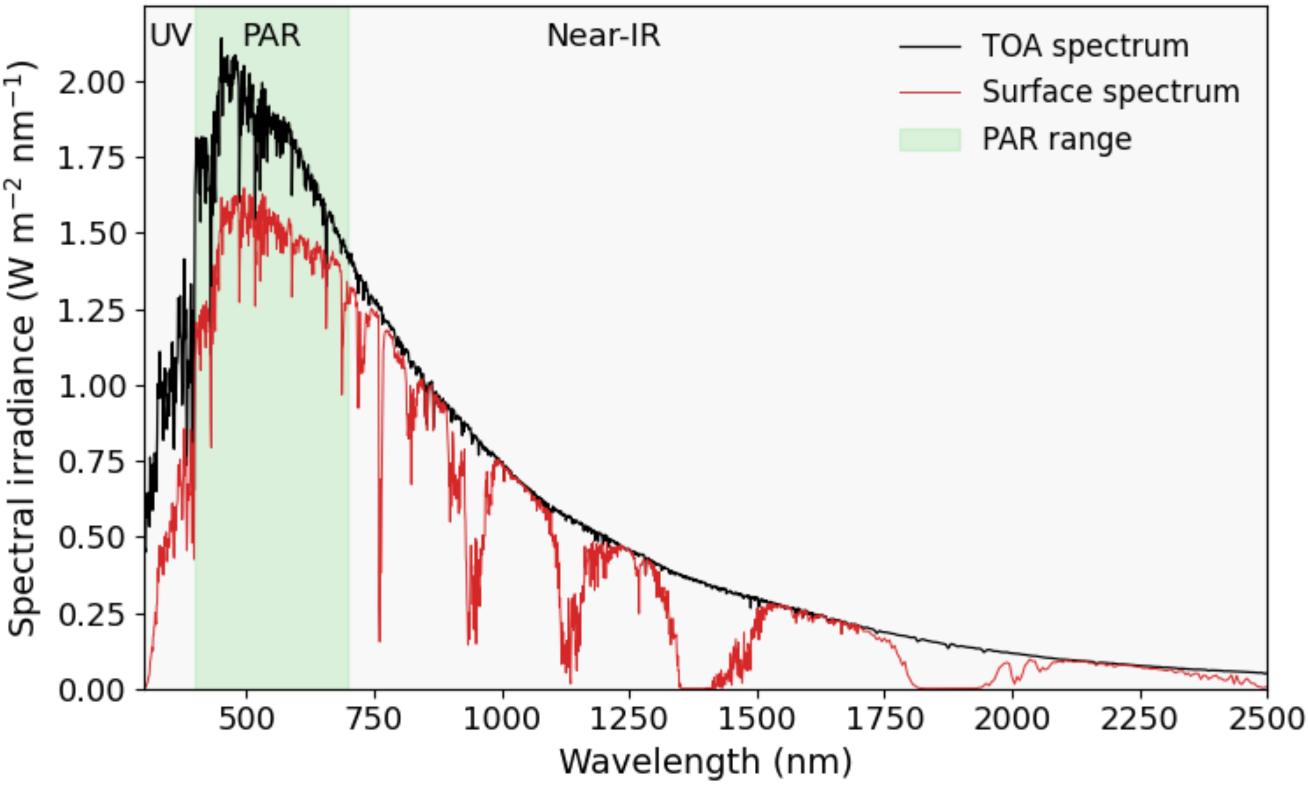

Figure 3: Solar spectral irradiance at the TOA and at the surface as a function of wavelength, showing the photosynthetically active radiation (PAR, 400–700 nm) range within the broader shortwave spectrum.

5.4 Global PAR as a closure solution

300 Please Using the definition of extraterrestrial PAR irradiance $I_{0,PAR}$, the surface global PAR can be written as

$$I_{PAR} = I_{0,PAR} k_{t,PAR} \; . \tag{12}$$

Applying the transmissivity mapping derived above gives the LC for global PAR,

$$I_{PAR} = I_{0,PAR} \, k_{t,SW}^{\alpha} \; . \tag{13}$$

This formulation preserves the physical bounds $0 < k_{t,SW} < 1$, ensures monotonicity, and maintains scale invariance in
305 transmissivity space. It constitutes the minimal non-trivial solution consistent with the multiplicative structure of atmospheric attenuation.

5.5 Diffuse PAR as a derived component

Diffuse PAR can be expressed as a fraction of global PAR,

$$I_{PAR,d} = I_{PAR} \, k_{d,PAR} \; , \tag{14}$$

310 where $k_{d,PAR}$ is the diffuse fraction in the PAR spectral range.

https://doi.org/10.5194/egusphere-2026-4728
Preprint. Discussion started: 8 September 2026
© Author(s) 2026. CC BY 4.0 License.

Similarly to the power-law governing the spectral mapping between SW and PAR (Equation 11) and additional power law emerges between diffuse fractions in both spectral ranges as

$$k_{d,\mathrm{PAR}} \approx k_{d,SW}^{\beta} \ , \tag{15}$$

where β > 0 is a dimensionless exponent. This formulation is introduced as a parsimonious closure-consistent representation of the spectral dependence of diffuse partitioning. Substituting in Equation 14 the global PAR closure (Equation 13) and the diffuse fraction mapping (Equation 15) yield the final expression for diffuse PAR,

$$\mathrm{I}_{PAR,d} = \mathrm{I}_{0,PAR}\, k_{t,SW}^{\alpha}\, k_{d.SW}^{\beta} \ . \tag{16}$$

In this formulation, diffuse PAR emerges as a derived quantity constrained by both broadband transmissivity and broadband diffuse partitioning, extending the closure consistently to the diffuse component.

5.6 Scope of the closure

The LC relies exclusively on broadband shortwave quantities and geometric factors embedded in extraterrestrial irradiance. All parameters are dimensionless and physically interpretable. The effective optical depths τ_B^{eff}, and consequently the exponents α and β, encapsulate departures from ideal monochromatic Beer–Lambert behaviour under real atmospheric conditions, including multiple scattering and cloud effects.

The closure admits a hierarchy of admissible solutions:

- The trivial solution α = 1 and β = 1,
- A constant non-trivial solution α ≠ 1 and β ≠ 1,
- Secondary modulation of LC

6 Evaluation of the Lozano Closure and Its Admissible Solutions

6.1 Evaluation framework and statistical metrics

The performance of the LC and its admissible solutions was evaluated across all study sites using a consistent statistical framework. The objective of this section is to analyse the admissible solutions of the model derived from the theoretical formulation presented in Section 5 and to evaluate their performance across sites.

Model performance is assessed using standard statistical indicators computed consistently across sites: the mean bias error (MBE), the relative root means square error (rRMSE, expressed as percentage of the mean observed value), and the coefficient of determination (r^2), whose formulations are summarised in Table 2. These metrics quantify, respectively, systematic bias, overall dispersion of residuals, normalised error magnitude, and explained variance. In addition, the statistical significance of the linear relationships was assessed using p-values, which are reported in the corresponding figures. For completeness, the number of valid data points (n) used in each evaluation is also reported in tables.

https://doi.org/10.5194/egusphere-2026-4728
Preprint. Discussion started: 8 September 2026
© Author(s) 2026. CC BY 4.0 License.

Table 2: Statistical performance metrics used.

Metrics	Equation
r^2	$\frac{\left(\sum_{i=1}^{n}[(x_i-\bar{x})(y_i-\bar{y})]\right)^2}{\sum_{i=1}^{n}(x_i-\bar{x})^2\sum_{i=1}^{n}(y_i-\bar{y})^2}$
MBE	$\frac{1}{n}\sum_{i=1}^{n}(y_i-x_i)$
rRMSE	$\frac{100}{\bar{x}}\sqrt{\frac{1}{n}\sum_{i=1}^{n}(y_i-x_i)^2}$
x_i experimental values y_i estimated values $\bar{x}$ mean of experimental values $\bar{y}$ mean of estimated values n number of values	

6.2 The trivial transmissivity solution (α = 1, β = 1)

This subsection evaluates the trivial solution of the LC, obtained by assuming that the broadband shortwave transmissivity provides a first-order proxy for PAR transmissivity, i.e. $k_{t,PAR} \approx k_{t,SW}$ (equivalently, α = 1). Under this assumption, global PAR is predicted as a TOA-scaled transmissivity product, and diffuse PAR is obtained by combining the global estimate with the broadband diffuse partitioning. The purpose of this analysis is to quantify (i) how far a purely transmissivity-driven, coefficient-free mapping can go across sites, and (ii) what residual structure remains when the closure is enforced in its simplest admissible form.

6.2.1 Global PAR performance across sites

Figure 4a shows measured versus modelled global PAR for the pooled multi-site dataset under the trivial solution. The relationship is strongly linear and physically constrained (non-negative, TOA-limited), indicating that most of the variance in surface global PAR is explained by the broadband transmissivity pathway. However, the regression line is systematically below the 1:1 line, consistent with a persistent negative bias of the trivial solution.

The site-level metrics (Table 3) confirm this behaviour. Across sites, the determination coefficient r^2 is consistently above 0.98, with relative error typically in the single-to-low-double digit range (rRMSE ≈ 6.9% – 21.5%). The bias is consistently negative at all sites (MBE ≈ -5 Wm^{-2} to -30 Wm^{-2}), indicating that the trivial mapping tends to underpredict PAR for a given broadband shortwave transmissivity. This sign-consistent bias is itself informative: it indicates a systematic spectral mismatch between broadband and PAR attenuation arising from the trivial solution, where identical effective attenuation is assumed for both bands despite the wavelength- dependent effects of clouds, aerosols, and atmospheric gases.

https://doi.org/10.5194/egusphere-2026-4728
Preprint. Discussion started: 8 September 2026
© Author(s) 2026. CC BY 4.0 License.

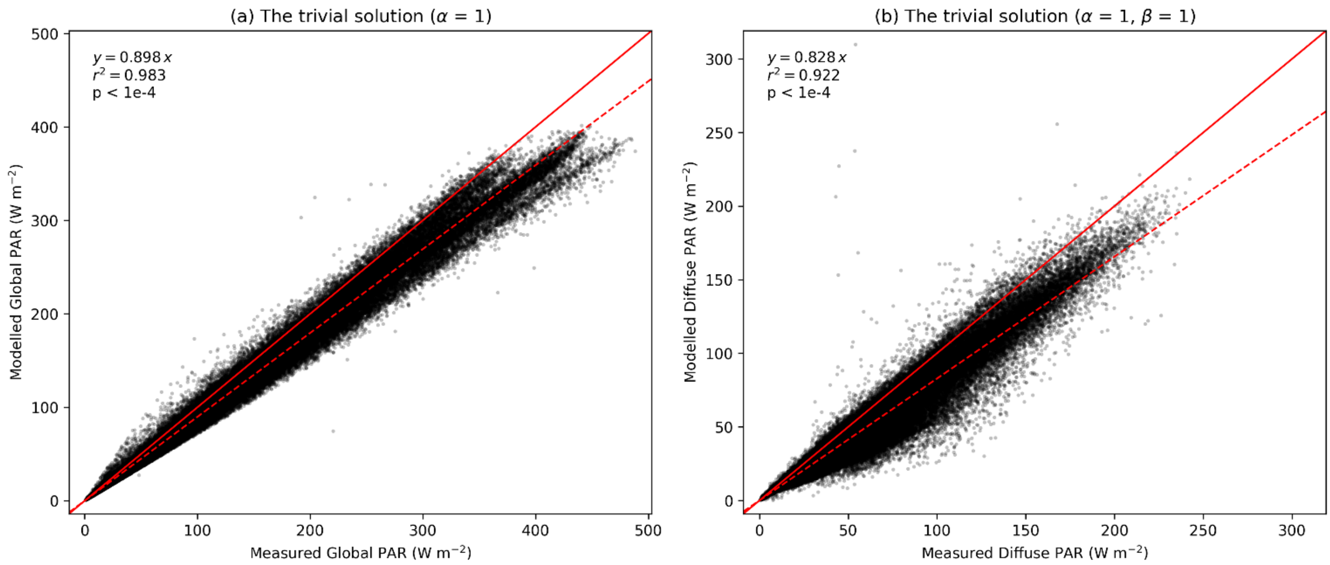

Figure 4: Measured versus modelled irradiance under the trivial solution of the LC for all sites combined: a) global PAR using α = 1 and b) diffuse PAR using α = 1, β = 1, for all sites combined. The solid red line denotes the 1:1 reference, and the dashed red line indicates the linear fit. Legend shows best linear fit, r^2, and p-value.

The corresponding multi-panel site plots (Appendix A Figure A1) show that this pattern is robust across ecosystems and climates, including croplands and forests, and across the two independent Spanish stations. The pooled scatter remains tight across most of the dynamic range, and the bias primarily manifests as a slope deviation rather than random dispersion, indicating that the effective spectral transmissivity mapping between broadband shortwave radiation and PAR is not unity in general.

Table 3: Statistical performance of LC for the trivial solution (α = 1), the non-trivial spectral exponent solution (α), and the air mass modulated exponent (α(m)), for global PAR across all study sites. Reported metrics include the number of valid observations (n), the mean bias error (MBE), the relative root means square error (rRMSE, expressed as percentage of the mean observed value), and the coefficient of determination (r^2).

Site	Solution	n	MBE (Wm^{-2})	rRMSE (%)	r^2
	α = 1		-4.8	6.9	0.994
DE-HoH	α	21738	1.9	5.4	0.995
	α(m)		2.6	5.8	0.995
	α = 1		-8.7	11.2	0.990
DE-Geb	α	14740	-1.7	8.5	0.989
	α(m)		-1.1	8.3	0.989
	α = 1		-5.1	8.0	0.994
DK-Vng	α	9232	1.6	6.2	0.994

https://doi.org/10.5194/egusphere-2026-4728
Preprint. Discussion started: 8 September 2026
© Author(s) 2026. CC BY 4.0 License.

	α(m)		2.3	6.4	0.994
FR-Fon	α = 1	19372	-21.3	17.3	0.993
	α		-14.0	13.0	0.995
	α(m)		-13.4	12.3	0.995
FR-Lam	α = 1	11954	-28.9	21.5	0.983
	α		-21.6	17.9	0.985
	α(m)		-20.9	17.4	0.985
SP-Gr	α = 1	2357	-26.1	12.1	0.997
	α		-16.8	8.5	0.997
	α(m)		-16.4	8.2	0.997
SP-Al	α = 1	4171	-30.3	13.2	0.994
	α		-21.6	10.0	0.995
	α(m)		-21.2	9.7	0.995

6.2.2 Diffuse PAR performance across sites

Diffuse PAR is a stricter test of the closure because it is not determined by transmissivity alone: it also depends on the physical partitioning between direct and diffuse radiation, which is sensitive specially to multiple scattering processes due to clouds and aerosols. Figure 4b shows measured versus modelled diffuse PAR under the trivial solution. Compared with global PAR, the scatter and the deviation from the 1:1 line is slightly larger, with dispersion increasing towards higher diffuse PAR values. The site-level statistics (Table 4) show r^2 values ranging from ≈ 0.871 to ≈ 0.979, and rRMSE typically between approximately 15.9% and 29.6%. Bias remains predominantly negative, with MBE spanning from -2.6 Wm^{-2} to -19.9 Wm^{-2}. Performance varies across sites, with the lowest rRMSE at DK-Vng (r^2 = 0.94, rRMSE ≈ 16%), and the largest at FR-Lam (r^2 = 0.87, rRMSE = 29.6%), illustrating that diffuse partitioning errors are more site- and regime-dependent than global transmissivity errors.

Table 4: Statistical performance of the LC for the trivial solution (α = 1, β = 1), the spectral mapping solution (α, β), and the air-mass-modulated solution (α(m), β) for diffuse PAR across all study sites. Reported metrics include the number of valid observations (n), the mean bias error (MBE), the relative root means square error (rRMSE, expressed as percentage of the mean observed value), and the coefficient of determination (r^2).

Site	Solution	n	MBE (Wm^{-2})	rRMSE (%)	r^2
DE-HoH	α = 1, β = 1	21737	-15.5	26.2	0.957
	α, β		-2.8	8.8	0.983
	α(m), β		-2.4	8.6	0.983

https://doi.org/10.5194/egusphere-2026-4728
Preprint. Discussion started: 8 September 2026
© Author(s) 2026. CC BY 4.0 License.

DE-Geb	α = 1, β = 1	14693	-12.7	25.2	0.927
	α, β		0.0	10.5	0.970
	α(m), β		0.4	10.6	0.969
DK-Vng	α = 1, β = 1	9228	-2.6	15.9	0.943
	α, β		9.2	21.4	0.976
	α(m), β		9.7	22.8	0.976
FR-Fon	α = 1, β = 1	6078	-9.9	17.6	0.954
	α, β		5.3	13.4	0.973
	α(m), β		5.9	14.5	0.974
FR-Lam	α = 1, β = 1	9933	-19.9	29.6	0.871
	α, β		-3.8	15.1	0.924
	α(m), β		-3.3	15.3	0.923
SP-Gr	α = 1, β = 1	2357	-17.3	18.3	0.979
	α, β		3.9	8.0	0.967
	α(m), β		4.0	8.3	0.966
SP-Al	α = 1, β = 1	4171	-18.0	21.6	0.953
	α, β		3.9	10.5	0.951
	α(m), β		4.0	10.7	0.950

Appendix A Figure A2 confirms that the dominant departure is again a systematic underestimation across most of the observed range, consistent with the interpretation that the trivial solution implicitly assumes $k_{d,PAR} \approx k_{d,SW}$ and a direct transfer of broadband partitioning into PAR. The residual diagnostics below show that this assumption is not strictly valid across the full range of atmospheric regimes.

6.2.3 Residual structure and physical interpretation

To move beyond aggregate skill metrics, Figure 5 diagnoses the normalised residuals of the trivial solution as a function of the key broadband drivers. The residuals are normalised by the PAR TOA irradiance (see Appendix B for site-by-site analysis), which isolates spectral/transmissivity effects from purely geometric scaling.

https://doi.org/10.5194/egusphere-2026-4728
Preprint. Discussion started: 8 September 2026
© Author(s) 2026. CC BY 4.0 License.

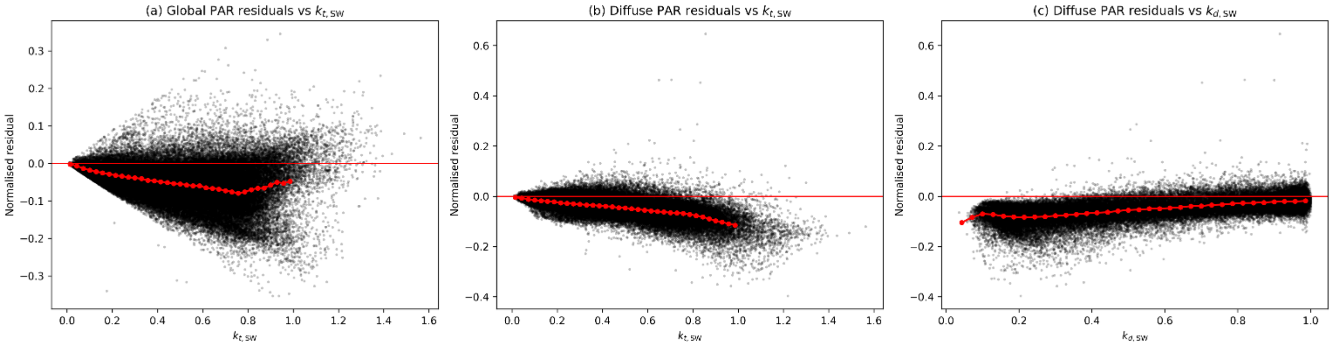

Figure 5: residuals of the trivial solution for all sites combined. Residuals are defined as (modelled – measured) / $I_{0,PAR}$: a) shows global PAR residuals vs $k_{t,SW}$, b) shows diffuse PAR residuals vs $k_{t,SW}$, while c) represent the diffuse PAR residuals vs $k_{d,SW}$. Black points represent individual observations; Red circles indicate bin-averaged values.

Global PAR residuals vs $k_{t,SW}$ (Figure 5a) show a clear, non-random structure: residuals are near zero at very low transmissivity (strongly attenuating conditions), but an increasing fraction become negative for intermediate-to-high $k_{t,SW}$, with the binned mean indicating a systematic drift away from zero. This behaviour is consistent with a spectral mapping effect: for a given SW transmissivity, the effective PAR transmissivity is not identical, and the mismatch projects as a multiplicative scaling error. The wedge-shaped pattern also indicates heteroscedasticity, expected when a single transmissivity proxy compresses a range of different spectral attenuation states (e.g., different aerosol/cloud mixtures).

Diffuse PAR residuals vs $k_{t,SW}$ (Figure 5b) show an even stronger monotonic tendency toward negative residuals as transmissivity increases. This indicates that, under clearer conditions (higher $k_{t,SW}$), the trivial solution increasingly underestimates diffuse PAR. Physically, this is consistent with the fact that diffuse PAR is not controlled solely by the magnitude of attenuation but by the scattering/absorption balance and angular redistribution, which broadband partitioning does not fully encode when directly transferred to PAR. The relatively small residuals observed under strongly attenuating conditions ($k_{t,SW} \leq 0.4$), typically associated with thick overcast cloud regimes (Ylivinkka et al., 2020), suggest that the LC is especially effective under conditions where the diffuse component dominates the radiation field.

Diffuse PAR residuals vs $k_{d,SW}$ (Figure 5c) exhibit structured curvature: a negative residual offset under low-to-moderate diffuse fraction and a gradual recovery toward less negative values as $k_{d,SW}$ increases. This reveals that the relationship between diffuse fraction in broadband SW and in the PAR band is not identity-like; rather, it behaves as a systematic mapping between spectral regimes. The tendency toward smaller residuals at high diffuse fractions is consistent with strongly overcast conditions, where the diffuse component dominates the radiation field and attenuation becomes more spectrally uniform across the shortwave and PAR domains. Importantly, the presence of an orderly trend supports the interpretation that a constrained functional transformation captures the dominant physics.

The appendix provides residual structure for each site (Appendix B Figures B1–B14), showing that these effects persist across locations but also highlight regime-specific features. In particular, some sites exhibit pronounced departures under high-albedo

https://doi.org/10.5194/egusphere-2026-4728
Preprint. Discussion started: 8 September 2026
© Author(s) 2026. CC BY 4.0 License.

states, suggesting that surface conditions and associated wintertime radiative regimes may influence the residual structure. The residuals also exhibit weaker but detectable dependencies on air mass and solar geometry (through θ and m).

6.3 The non-trivial solution

The closure exponents were estimated directly from the transmissivity mappings implied by Section 5 Equations 11 and 15, using a log–log linear fit (equivalently, fitting $\ln k_{t,PAR} = \alpha \ln k_{t,SW}$ and $\ln k_{d,PAR} = \beta \ln k_{d,SW}$) over the quality-controlled dataset. A random 75% subset of the pooled multi-site data was used to estimate both exponents, and the remaining 25% subset was used for verification. The resulting $\alpha = 0.9088$ ($r^2 = 0.971$) and $\beta = 0.7855$ ($r^2 = 0.923$) were fixed as a single cross-site value for all subsequent model evaluations.

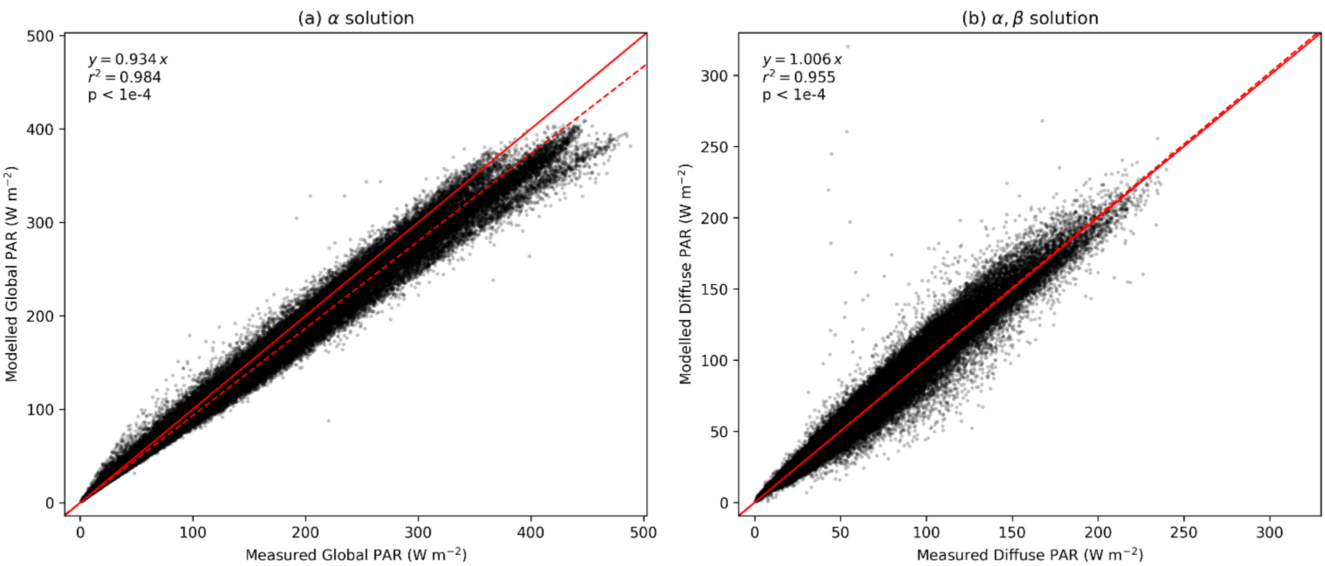

Figure 6: Measured versus modelled global and diffuse PAR under the non-trivial solution of the LC for all sites combined: a) α solution and b) α, β solution. The red solid line denotes the 1:1 reference, and the dashed red line indicates the linear fit. Reported values correspond to the fitted slope, r^2, and p-value.

6.3.1 Global PAR under the non-trivial solution

Figure 6a shows measured versus modelled global PAR obtained when all sites are pooled. Comparing with the trivial solution, which exhibits a slightly lower r^2 value (0.983 vs 0.984 for the non-trivial solution), the deviation between the fitted line and the 1:1 reference is reduced, and the slope approaches unity, indicating a reduction in systematic bias.

This behaviour is consistent with the site-by-site metrics reported in Table 3, where all stations show a clear reduction in MBE and rRMSE. The r^2 values range from 0.985 (FR-Lam) to 0.997 (SO-Gr) confirming the improved performance of the non-trivial solution across contrasting climatic and surface conditions.

The corresponding site-by-site scatter plots are presented in Appendix A Figure A3. Sites that previously showed stronger slope deviations under the trivial solution (e.g., FR-Lam and SP-Al) display a marked correction of the systematic offset while

https://doi.org/10.5194/egusphere-2026-4728
Preprint. Discussion started: 8 September 2026
© Author(s) 2026. CC BY 4.0 License.

maintaining high explained variance. Across all stations, the scatter remains tightly organised along a single linear structure, indicating that the exponent α primarily adjusts the broadband-to-PAR transmissivity scaling without altering the variance structure.

These results are consistent with the interpretation that α captures a stable spectral transmissivity relationship between SW and PAR.

6.3.2 Diffuse PAR under the non-trivial solution

Diffuse PAR is obtained by combining the transmissivity exponent α with the diffuse-partition exponent β, as presented in Equation (16). The pooled evaluation (Figure 6b) yields $r^2 = 0.955$, representing an improvement over the trivial solution ($r^2 = 0.922$), with fitted line closely aligned with the 1:1 reference, indicating that the systematic bias observed in the trivial solution is largely removed. The linear alignment between measured and modelled diffuse PAR is preserved across the full range of conditions.

Site-wise diagnostics (Table 4 and Appendix A Figure A4) show slopes close to unity for most stations, including DE-Geb (0.994), SP-Gr (1.031), and SP-Al (1.026). The r^2 values range from 0.924 (FR-Lam) to 0.983 (DE-HoH). Moderate deviations remain at some locations (e.g., DK-Vng with slope 1.153 and FR-Fon with 1.079), reflecting local variability in diffuse partitioning. Nevertheless, the combined exponent solution eliminates the persistent structural offset present under the trivial solution and substantially improves cross-site consistency.

6.4 Secondary geometric modulation

The residual analyses presented in Section 6.2 and Appendix B indicate that, although the non-trivial solution captures the dominant transmissivity structure, small systematic slope deviations persist at some stations. These deviations suggest that the effective spectral mapping exponent may not be strictly invariant across all geometric regimes. In principle, several factors could contribute to such residual structure, including aerosol variability, cloud optical properties, surface albedo, gas absorption features, or geometric effects related to optical path length.

However, introducing additional atmospheric predictors would depart from the structural philosophy of the LC, which seeks to express PAR solely as a transmissivity mapping derived from broadband shortwave radiation. Therefore, instead of incorporating new independent variables, we restrict the analysis to testing whether purely geometric factors (already implicit in the definition of transmittance) can account for part of the remaining residual structure.

Within the Beer–Lambert representation (Equation 6), attenuation depends on the product of τ and m. Under this interpretation, the exponent α in the relation on Equation 15 may be viewed as a band-effective optical-depth ratio. Because air mass increases nonlinearly at large zenith angles, small departures from a strictly constant α could emerge under extreme geometric conditions without requiring additional atmospheric state variables.

https://doi.org/10.5194/egusphere-2026-4728
Preprint. Discussion started: 8 September 2026
© Author(s) 2026. CC BY 4.0 License.

To explore this possibility in a controlled and bounded manner, we define a mean-preserving geometric modulation of the exponent:

$$\alpha(m) = \alpha_0[1 + \varepsilon g(m)] \,, \quad (17)$$

with

$$g(m) = \tanh(\ln m - \ln \overline{m}) \,, \quad (18)$$

where α_0 is the globally estimated exponent from Section 6.3, $\overline{m}$ is the mean air mass of the analysed dataset, and ε controls the amplitude of the modulation. The hyperbolic tangent ensures bounded corrections ($| g(m) | < 1$), so that α(m) remains close to α_0 and only deviates under large air-mass departures. This formulation preserves the closure structure and avoids introducing unbounded or site-dependent corrections.

Air mass was computed from solar zenith angle using the standard Kasten and Young (1989) optical-air-mass approximation. The modulation amplitude ε was evaluated over a small physically conservative range [0.01, 0.1] and then fixed at ε = 0.05. This formulation allows assessment of whether weak geometric scaling alone can explain part of the residual structure while maintaining the universality and minimal-variable philosophy of the closure.

6.4.1 Global PAR under geometric modulation

Figure 7a presents measured versus modelled global PAR using the geometrically modulated exponent α(m). When all stations are pooled, the forced-origin fit yields a slope of 0.939 with $r^2 = 0.984$, essentially unchanged relative to the fixed-α solution in terms of explained variance. The primary effect of the modulation is a slight adjustment of the regression slope toward the 1:1 reference, indicating a modest reduction in systematic scaling deviations.

At the site level (Appendix A Figure A5), slope adjustments are small but structured. For example, DE-HoH and DK-Vng exhibit slopes close to unity (1.013 and 1.007, respectively), while SP-Gr and FR-Lam show minor shifts relative to the fixed-α configuration. The overall dispersion structure remains unchanged, and r^2 values remain unchanged compared with the α-solution, however the sites with the higher bias shows a slight correction.

These results suggest that weak optical-path effects may contribute marginally to cross-site slope differences in global PAR, but the dominant transmissivity mapping remains captured by the constant exponent formulation.

https://doi.org/10.5194/egusphere-2026-4728
Preprint. Discussion started: 8 September 2026
© Author(s) 2026. CC BY 4.0 License.

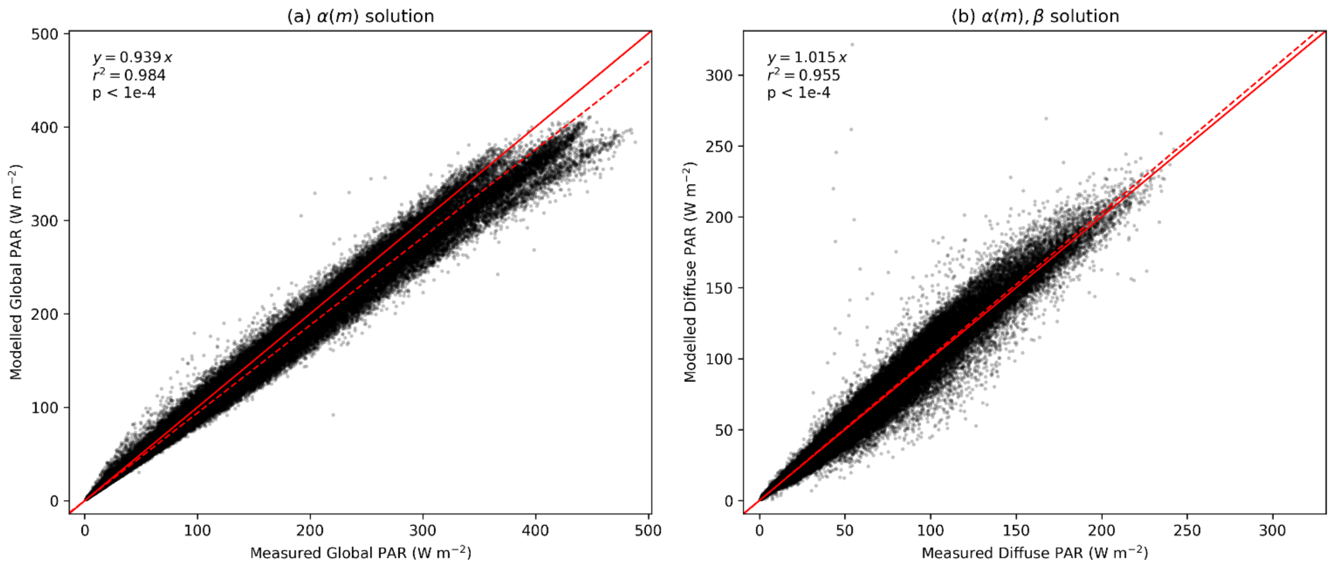

Figure 7: Measured versus modelled global and diffuse PAR under the α(m) solution of the LC for all sites combined. The red solid line denotes the 1:1 reference, and the dashed red line indicates the linear fit. Reported values correspond to the fitted slope, r^2, and p-value.

6.4.2 Diffuse PAR under geometric modulation

The behaviour for diffuse PAR differs from that observed for global PAR. Figure 7b shows the pooled evaluation under the combined α(m) and β formulation, yielding $r^2 = 0.955$, comparable to the fixed-exponent solution. However, alignment between the fitted slope and the 1:1 reference is marginally weaker relative to Section 6.3.

Site-wise diagnostics (Appendix A Figure A6) confirm this asymmetry. While some stations (e.g., DE-HoH, FR-Lam) show marginal slope adjustments toward unity, others display slight divergence compared with the fixed-α solution. For example, DK-Vng and FR-Fon retain noticeable deviations, and in certain cases the slope alignment is slightly less consistent than in the constant-exponent configuration. The r^2 values remain within the same range as previously reported (0.923–0.983), indicating that the geometric modulation does not materially change the explanatory power for diffuse PAR.

This behaviour indicates that residual variability in diffuse partitioning is not primarily governed by geometric optical-path scaling alone. Instead, it likely reflects site-specific atmospheric and cloud-related processes that are not captured by a purely transmissivity-based modulation of α.

7 Discussion

7.1 Physical interpretation of the spectral exponent α

The spectral exponent α derived in Section 6 can be interpreted as an effective ratio of band-integrated optical depths, linking SW transmissivity to PAR transmissivity. Within the Beer–Lambert framework (Equation 6), attenuation depends on the

https://doi.org/10.5194/egusphere-2026-4728
Preprint. Discussion started: 8 September 2026
© Author(s) 2026. CC BY 4.0 License.

product of wavelength-dependent optical depth and optical air mass (Chandrasekhar, 2013; Iqbal, 1983; Liou, 2002). When integrated over spectral bands, differences in extinction efficiency between the PAR range (400 - 700 nm) and the broader shortwave spectrum give rise to a systematic scaling relationship between their corresponding transmissivities. The exponent α therefore represents a band-effective optical-depth ratio, encapsulating the relative spectral weighting of extinction processes across the two bands.

The estimated value (α = 0.9088) indicates that, on average, the effective attenuation in the PAR band scales slightly less strongly than SW attenuation (Bird and Hulstrom, 1981; Bird and Riordan, 1986; Gueymard, 1989; Kato et al., 1999). This behaviour is physically consistent with the spectral structure of atmospheric extinction (Gueymard, 2003; Van Laake and Sanchez-Azofeifa, 2005). Broadband shortwave radiation includes near-infrared wavelengths where molecular absorption, particularly by water vapour, contributes significantly, whereas the PAR band lies primarily within a spectral region where absorption is weaker and extinction is dominated by scattering processes (Liou, 2002; Wen et al., 2008). Although scattering is more efficient at shorter wavelengths, its spectral dependence differs from that of gaseous absorption, leading to a distinct weighting of extinction across the solar spectrum. As a result, SW transmissivity integrates absorption features not present within the PAR band, naturally yielding an exponent smaller than unity when expressed as a power-law mapping.

A key result of the multi-site evaluation is the quasi-stationary character of α. Despite the diversity of climatic regimes represented in the dataset including Mediterranean aerosol-influenced conditions, central European croplands, and northern temperate forests, the exponent remains stable when estimated from pooled data. This suggests that α primarily reflects fundamental spectral differences between extinction processes rather than site-specific meteorological variability. Because the clearness index $k_{t,SW}$ already integrates the combined effects of aerosols, clouds, and gases (Iqbal, 1983; Jung et al., 2016; Kim et al., 2020), the spectral mapping effectively operates on a transmissivity that has collapsed much of the atmospheric state dependence into a single dimensionless quantity.

The limited impact of the secondary geometric modulation introduced in Section 6.4 further supports this interpretation. While optical path length influences instantaneous attenuation through the air-mass factor (Noll et al., 2012), the exponent itself appears largely invariant to moderate geometric variations. The weak sensitivity observed under extreme air-mass conditions is consistent with second-order optical-depth effects, but does not alter the dominant band-to-band scaling captured by the constant exponent formulation.

Taken together, these results indicate that α is a band-integrated descriptor of spectral attenuation differences between PAR and SW. Its stability across sites and regimes underpins the structural robustness of the closure.

7.2 Diffuse partitioning and the physical meaning of β

Unlike the spectral exponent α, which primarily reflects band-integrated differences in total extinction between PAR and broadband shortwave radiation, the exponent β governs the mapping between SW and PAR diffuse fractions, and is therefore directly linked to scattering processes and angular redistribution of radiation.

https://doi.org/10.5194/egusphere-2026-4728
Preprint. Discussion started: 8 September 2026
© Author(s) 2026. CC BY 4.0 License.

Diffuse irradiance arises from multiple scattering by molecules, aerosols, and cloud droplets. Its magnitude depends not only on the integrated optical depth, but also on single-scattering albedo, phase function asymmetry, cloud optical depth, and surface albedo feedbacks (Kokhanovsky, 2006; Liou, 2002). Consequently, the partition between direct and diffuse radiation is inherently more sensitive to microphysical and cloud-structural properties than total transmissivity alone (Kikuchi et al., 2006; Meyer et al., 2004).

The estimated value $\beta \approx 0.79$ indicates a sublinear relationship between diffuse fractions in the PAR and SW ranges when expressed through the power-law mapping. This behaviour reflects the stronger relative contribution of scattering processes at shorter wavelengths, which enhances the diffuse component in the PAR range compared to SW radiation. As a result, spectral differences in extinction lead to a systematically different scaling between PAR and SW diffuse fractions.

Physically, this reflects the wavelength dependence of scattering and absorption processes: molecular (Rayleigh) scattering is more efficient at shorter wavelengths within the PAR band, while absorption features in the near-infrared contribute more strongly to SW attenuation (Ångström, 1964; Bird and Hulstrom, 1981; Gueymard, 2004). In cloudy conditions, the spectral dependence of cloud optical properties and droplet effective radius further modifies this partitioning (Hu and Stamnes, 1993; Slingo, 1989; Stephens, 1978). Aerosols introduce an additional spectral component, particularly when absorbing species such as brown carbon or mineral dust are present, altering diffuse fractions differently across spectral bands (Chakrabarty et al., 2023; Chen et al., 2022).

These mechanisms explain why β exhibits greater site-to-site dispersion than α in the empirical evaluation. While total transmissivity tends to collapse into a relatively stable bulk measure through the clearness index, diffuse partitioning depends more strongly on local aerosol composition, cloud climatology, and humidity-driven changes in particle size distribution (Gueymard, 2012; Ramanathan et al., 1989, 2001). In a more general formulation, the diffuse exponent can therefore be conceptualised as

$$\beta = f(AOD, COD, SSA, RH, albedo, \dots) , \quad (19)$$

where AOD denotes aerosol optical depth, COD cloud optical depth, SSA single-scattering albedo, RH relative humidity, and surface albedo influences multiple scattering.

However, explicitly parameterising β as a multivariate function would introduce additional predictors that reduce the universality and transferability of the closure. The guiding principle of the present formulation is to derive a spectrally consistent, TOA-normalised mapping that operates without site-specific calibration or auxiliary atmospheric inputs. Under this constraint, a stationary cross-site estimate of β captures the dominant average spectral-partition behaviour while preserving structural simplicity.

The empirical results show that this reduced formulation substantially removes the structural offset present in the trivial solution and achieves consistent alignment across climatic regimes, even though moderate deviations remain at sites characterised by strong local diffuse variability. These residual differences are physically interpretable within the broader functional dependence described above and point toward future extensions of the closure in which β may be allowed to vary

https://doi.org/10.5194/egusphere-2026-4728
Preprint. Discussion started: 8 September 2026
© Author(s) 2026. CC BY 4.0 License.

conditionally when additional atmospheric state variables are available. Thus, β should be interpreted as a band-effective diffuse partition descriptor under the universality constraint adopted in this work.

7.3 Comparison with existing PAR modelling approaches

A substantial body of literature has addressed the estimation of PAR from SW or satellite-derived irradiance products. These approaches generally fall into three categories: empirical kt-based parameterisations, multivariate and machine-learning models, and satellite-driven TOA-normalised frameworks.

Empirical models for PAR have traditionally expressed global PAR as a function of broadband irradiance and atmospheric indices such as clearness index, diffuse fraction, or solar elevation angle. Early formulations based on ground measurements (e.g., Alados and Alados-Arboledas, 1999a, b) demonstrated the feasibility of estimating both global and diffuse PAR using empirical relationships, but also highlighted the need for site-specific calibration to maintain accuracy under varying atmospheric conditions.

More recent studies have extended these approaches using larger datasets and satellite-derived inputs. Ferrera-Cobos et al. (2020) reported daily PAR estimation errors in the range of rRMSE ≈ 8 - 15% with some models reaching values above 30%, with improvements achieved through site-specific adaptation techniques. Vindel et al. (2018), using satellite-derived inputs over mainland Spain, obtained r^2 values typically between 0.994 and 0.998 and rRMSE from ≈ 2 – 10 % depending on region and sky conditions. These studies confirm the strong coupling between PAR and broadband transmissivity, but also show that calibration or regional tuning is often required to maintain performance across climatic regimes. Ma Lu et al. (2024), focusing on high-latitude diffuse separation, reported r^2 values around 0.85 - 0.94, with rRMSE values ranging approximately from 12 % to 22% for diffuse PAR depending on season and solar geometry.

Machine-learning approaches further reduce statistical error by incorporating multiple predictors or nonlinear mappings. In the empirical and ANN comparison presented in Lozano et al. (2023), diffuse PAR estimation achieved r^2 up to ≈ 0.99 for site-specific models, although performance varied when applied outside the calibration domain. These results demonstrate that high predictive skill can be achieved when flexible models are trained locally, but also underline the dependence of such methods on data availability and regional tuning.

Satellite-based formulations introduce TOA-normalised structures more closely related to the philosophy of the present closure. Van Laake and Sanchez-Azofeifa (2004) reported r^2 = 0.99 for daily estimation of direct PAR for MODIS-based mapping, while Janjai and Wattan (2011) achieved r^2 = 0.96 for global PAR using geostationary satellite-based models after empirical corrections. These studies demonstrate the effectiveness of TOA-referenced formulations, though most require explicit retrieval of cloud and atmospheric parameters or region-specific adjustments.

Against this background, the LC achieves, for global PAR, pooled r^2 ≈ 0.98 - 0.99 with rRMSE typically in the 5–13% range across diverse climatic regimes without site-specific calibration. For diffuse PAR, r^2 values range from ≈ 0.92 to 0.98 across sites, with rRMSE generally below ~15% under the stationary β formulation. These values lie within the performance envelope reported for calibrated empirical and ANN-based models.

https://doi.org/10.5194/egusphere-2026-4728
Preprint. Discussion started: 8 September 2026
© Author(s) 2026. CC BY 4.0 License.

A key distinction, however, lies in structural requirements. Many empirical formulations rely on regionally adapted coefficients or multi-parameter regressions, while ANN approaches require extensive local training datasets to achieve their highest accuracy. Satellite-based TOA frameworks frequently involve explicit retrieval of cloud or aerosol parameters and, in several cases, focus primarily on global or direct PAR rather than diffuse partitioning. In contrast, the LC employs a single transmissivity-based mapping driven only by broadband irradiance and solar geometry, without local tuning, auxiliary meteorological inputs, or training procedures.

Under this minimal-input configuration, the closure attains performance levels comparable to the most accurate calibrated models, while maintaining cross-site transferability and explicit physical interpretability. The advantage of the approach therefore resides not in statistical optimisation through additional predictors, but in the capacity to preserve universality and spectral consistency within a compact TOA-normalised framework.

A further structural advantage of the LC is that global and diffuse PAR are derived consistently within a single transmissivity-based framework. In many existing approaches, global and diffuse components are treated through separate parameterisations or independent modelling strategies, often requiring distinct calibration procedures. In contrast, the present formulation links both components through the same TOA-normalised spectral mapping, ensuring internal coherence between total transmissivity and diffuse partitioning. This unified treatment reinforces the physical consistency of the closure while preserving its cross-site applicability.

8 Implications and future directions

8.1 Structural implications for large-scale application

The results indicate that a spectrally consistent PAR reconstruction can be achieved from broadband shortwave radiation using a minimal TOA-normalised transmissivity mapping. Because the formulation requires no site-specific calibration or auxiliary atmospheric predictors, it is directly transferable across climatic regimes. This structural simplicity makes the closure particularly suited for applications where only broadband irradiance and solar geometry are available, including operational networks and large-scale gridded products.

8.2 Sensitivity to extraterrestrial spectral normalisation

A sensitivity analysis was conducted to assess the dependence of the spectral exponent α on the adopted extraterrestrial PAR normalisation. Replacing the baseline PAR solar constant (Gueymard, 2018) with an alternative value historically used in earlier formulations (Iqbal, 1983) produced a systematic shift in model behaviour when α was held fixed, with a marked degradation in performance across sites. Re-estimating α under the modified solar constant partially restored performance but resulted in a systematic shift of the inferred exponent from $\alpha \approx 0.91$ to $\alpha \approx 1.04$ and increased site-to-site dispersion.

These results indicate that α encodes the spectral mapping between broadband and PAR transmittances conditional on the adopted extraterrestrial spectral reference. This finding highlights the importance of coherent extraterrestrial normalisation for

https://doi.org/10.5194/egusphere-2026-4728
Preprint. Discussion started: 8 September 2026
© Author(s) 2026. CC BY 4.0 License.

universal application of transmissivity-based models. Future work should evaluate the use of satellite-derived top-of-atmosphere spectral irradiance products to further constrain α and quantify the impact of solar-constant uncertainties on regional and large-scale PAR estimation.

8.3 Extension of the diffuse partition formulation

Future developments may allow β to vary conditionally with aerosol and cloud properties when additional atmospheric data are available, enabling regime-dependent refinement beyond the stationary universal formulation adopted here.

8.4 Broader applications and spectral generalisation

Although the present work focuses on PAR, the formulation is not intrinsically limited to this spectral band. The transmissivity-based mapping derived in Section 5 can, in principle, be extended to other spectral intervals provided that consistent TOA-normalised definitions are available. This opens the possibility of developing analogous closures for ultraviolet, near-infrared, or other sub-bands relevant to radiative forcing and biosphere–atmosphere coupling.

In Earth system modelling contexts, where radiative inputs often rely on broadband parameterisations, a spectrally coherent closure offers a pathway to reconstruct sub-band radiation fields without introducing additional empirical regressions. Such extensions would contribute to reducing structural inconsistencies between broadband forcing estimates and biologically relevant spectral fluxes.

9 Conclusions

This study introduced the Lozano Closure, a physically constrained, TOA-normalised transmissivity framework linking broadband shortwave radiation (SW) and photosynthetically active radiation (PAR). The formulation expresses global and diffuse PAR as spectral mappings of broadband transmissivity through two band-integrated exponents, α and β, derived from log–log transmissivity relations.

The trivial transmissivity solution ($\alpha = 1$) captures a large fraction of global PAR variability, but systematic slope deviations indicate that broadband and PAR transmissivities are not equivalent. Introducing the spectral exponent α removes this structural bias and yields r^2 up to 0.997 for global PAR across diverse climatic regimes without site-specific calibration. Diffuse PAR, governed by the additional exponent β, achieves r^2 values between ≈ 0.92 and 0.98 across sites, substantially improving partition consistency relative to the trivial formulation.

The spectral exponent α exhibits quasi-stationary behaviour across climates, consistent with its interpretation as a band-effective optical-depth ratio. In contrast, β reflects the greater regime sensitivity of diffuse partitioning. Sensitivity experiments further demonstrate that α is structurally conditioned by the adopted extraterrestrial spectral normalisation, underscoring the importance of coherent TOA definitions for universal application.

https://doi.org/10.5194/egusphere-2026-4728
Preprint. Discussion started: 8 September 2026
© Author(s) 2026. CC BY 4.0 License.

Compared with empirical, ANN-based, and satellite-driven approaches, the LC achieves competitive performance using only SW irradiance and solar geometry, without local calibration or auxiliary atmospheric predictors. Its principal contribution lies in providing a minimal, spectrally consistent, and transferable framework for reconstructing both global and diffuse PAR.

Although the present work focuses on PAR, the transmissivity-based formulation is extensible to other spectral bands. The closure therefore offers a pathway toward spectrally coherent sub-band reconstruction within broadband radiation frameworks.

Appendix A Validation figures

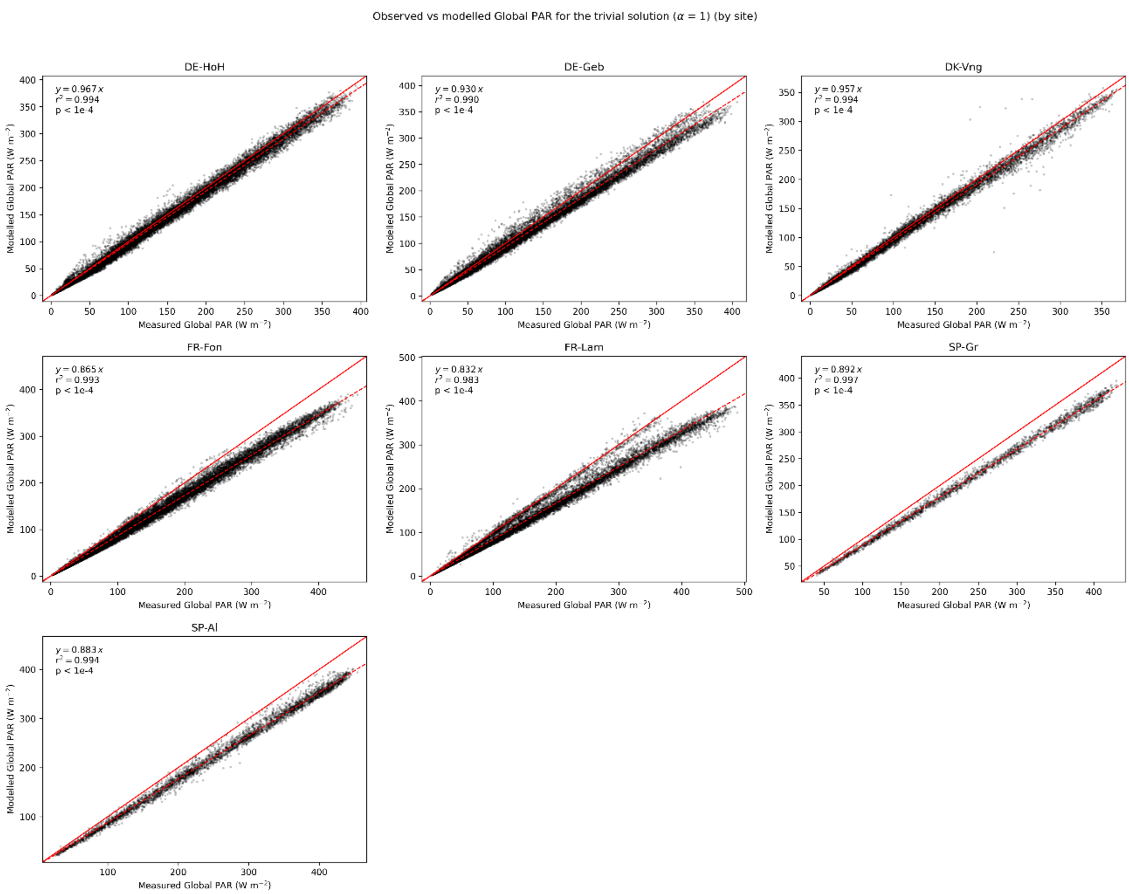

https://doi.org/10.5194/egusphere-2026-4728
Preprint. Discussion started: 8 September 2026
© Author(s) 2026. CC BY 4.0 License.

Figure A1. Measured versus modelled global PAR under the trivial solution (α = 1) for all study sites. The red solid line denotes the 1:1 reference, and the dashed red line indicates the linear fit. Reported values correspond to the fitted slope, r^2, and p-value.

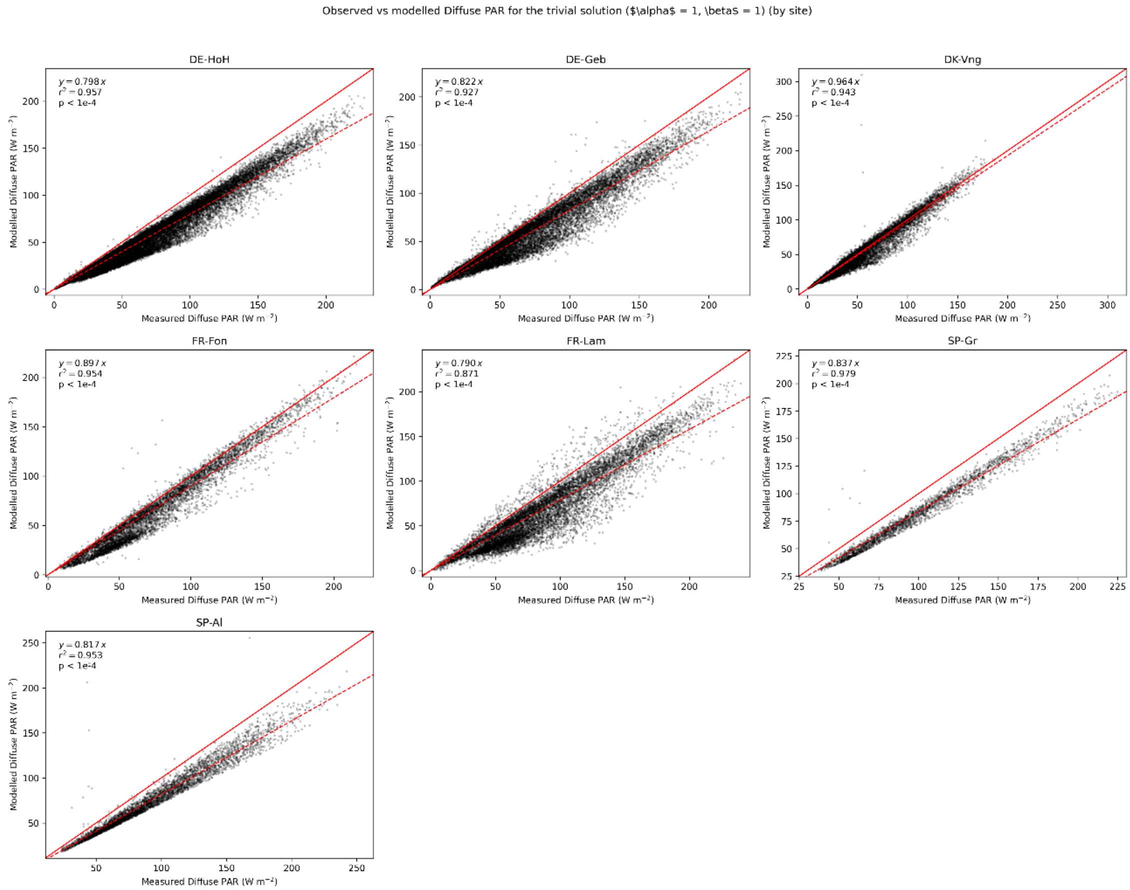

Figure A2. Measured versus modelled diffuse PAR under the trivial solution (α = 1, β = 1) for all study sites. The red solid line denotes the 1:1 reference, and the dashed red line indicates the linear fit. Reported values correspond to the fitted slope, r^2, and p-value.

https://doi.org/10.5194/egusphere-2026-4728
Preprint. Discussion started: 8 September 2026
© Author(s) 2026. CC BY 4.0 License.

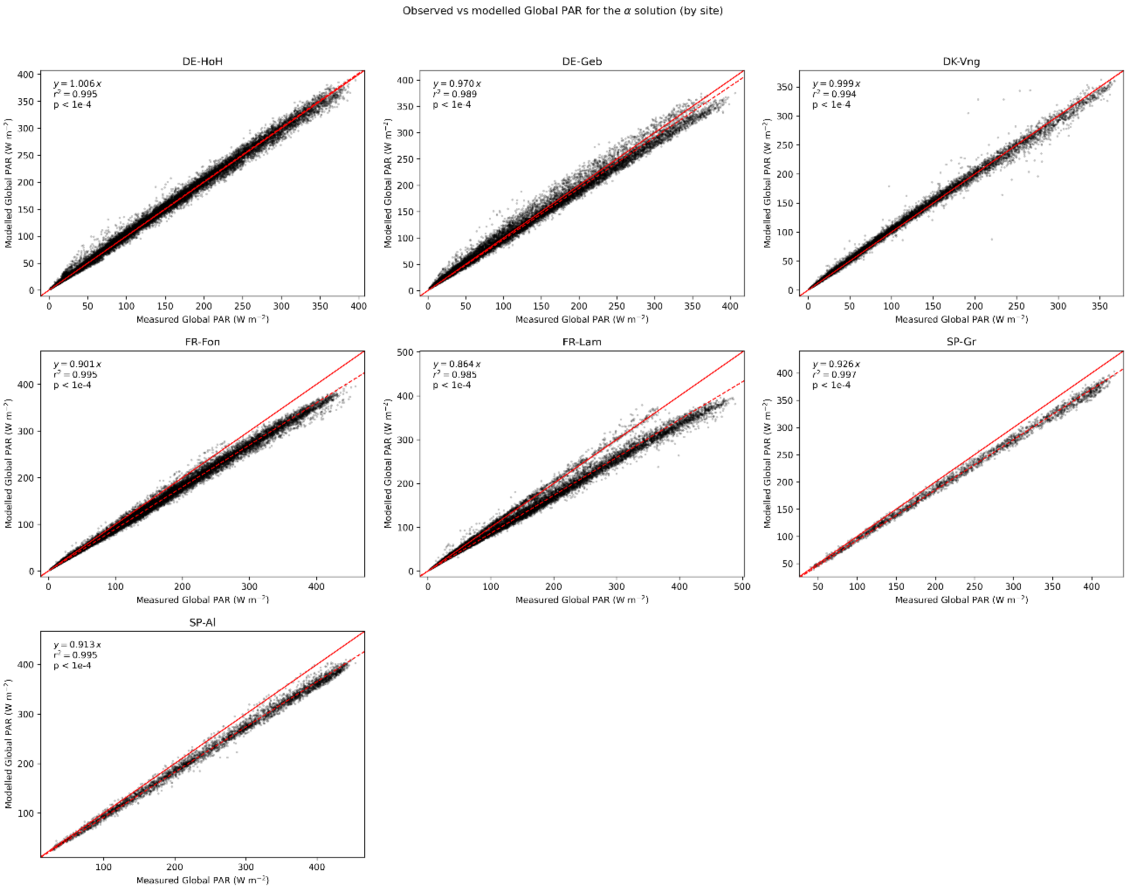

Figure A3. Measured versus modelled global PAR under the non-trivial solution ($\alpha \neq 1$) for all study sites. The red solid line denotes the 1:1 reference, and the dashed red line indicates the linear fit. Reported values correspond to the fitted slope, r^2, and p-value.

https://doi.org/10.5194/egusphere-2026-4728
Preprint. Discussion started: 8 September 2026
© Author(s) 2026. CC BY 4.0 License.

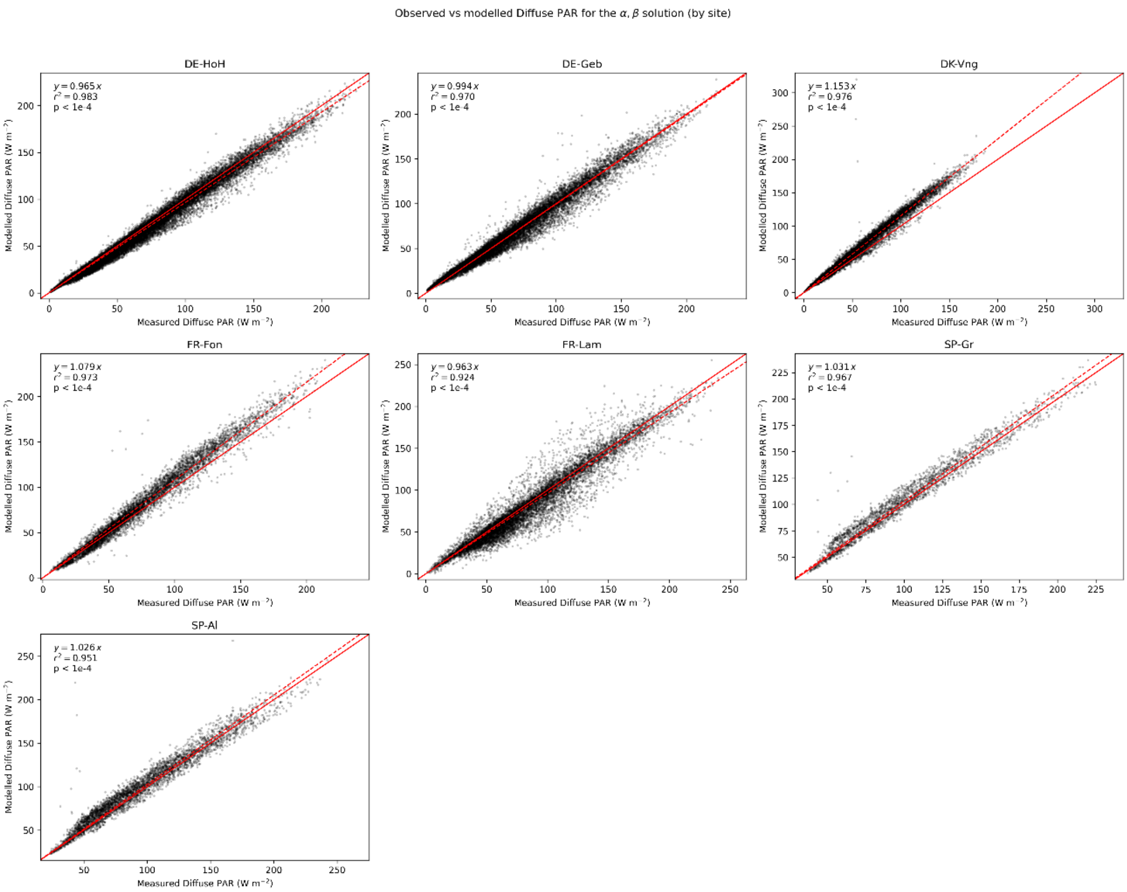

Figure A4. Measured versus modelled diffuse PAR under the non-trivial solution (α, β ≠ 1) for all study sites. The red solid line denotes the 1:1 reference, and the dashed red line indicates the linear fit. Reported values correspond to the fitted slope, r^2, and p-value.

https://doi.org/10.5194/egusphere-2026-4728
Preprint. Discussion started: 8 September 2026
© Author(s) 2026. CC BY 4.0 License.

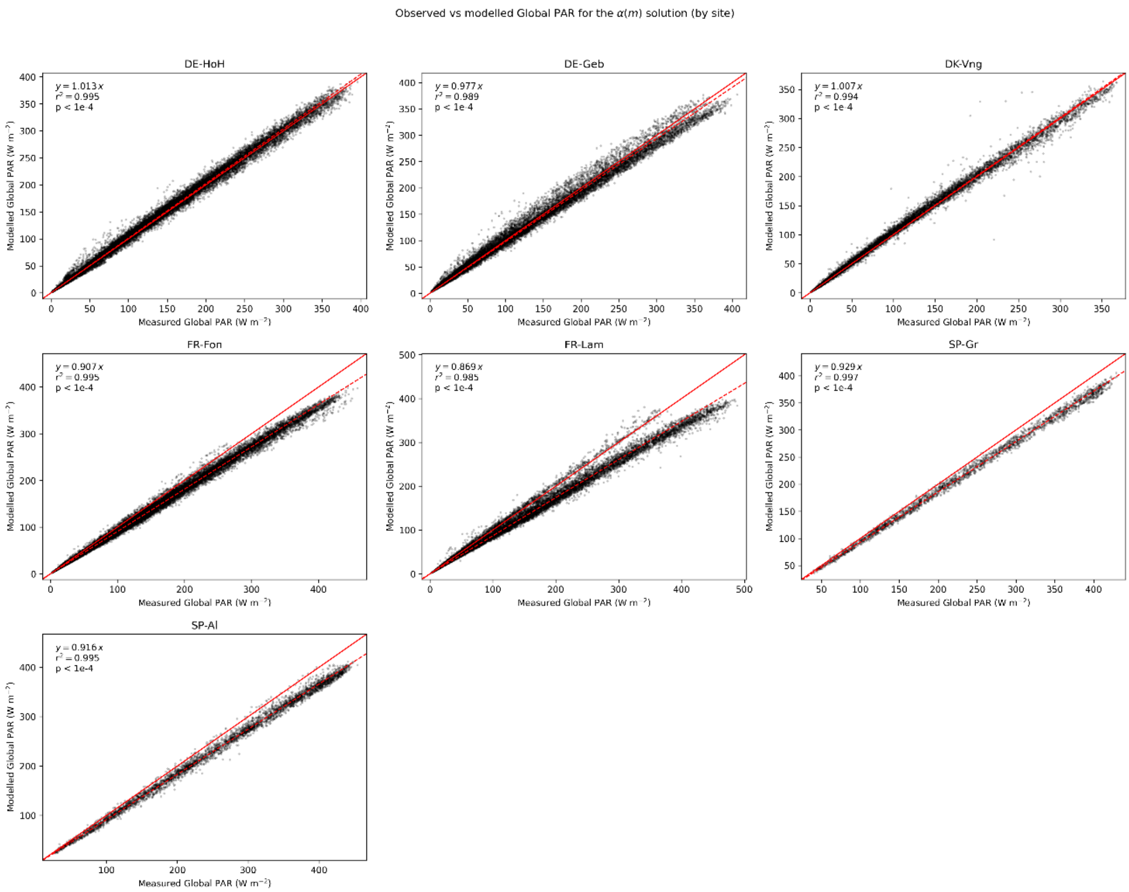

Figure A5. Measured versus modelled global PAR under secondary geometric modulation α(m) for all study sites. The red solid line denotes the 1:1 reference, and the dashed red line indicates the linear fit. Reported values correspond to the fitted slope, r^2, and p-value.

https://doi.org/10.5194/egusphere-2026-4728
Preprint. Discussion started: 8 September 2026
© Author(s) 2026. CC BY 4.0 License.

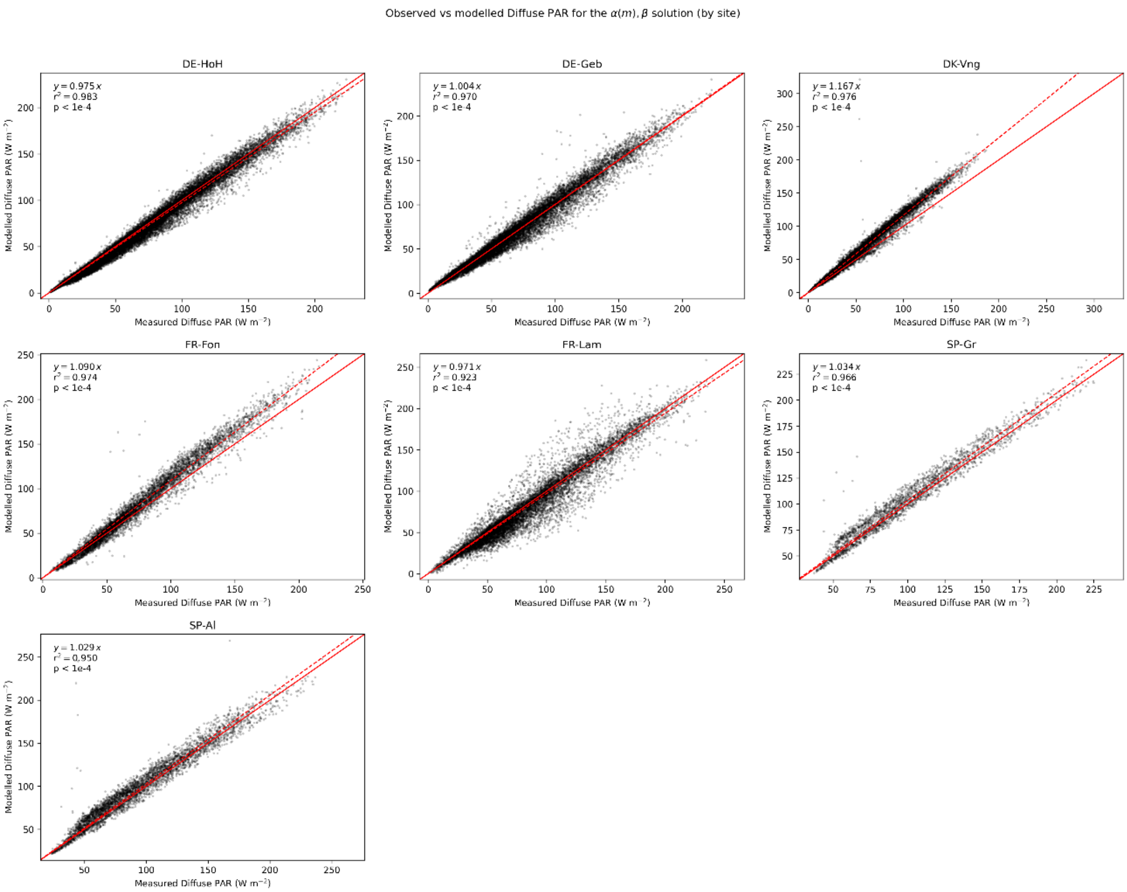

Figure A6. Measured versus modelled diffuse PAR under secondary geometric modulation α(m) with stationary β for all study sites. The red solid line denotes the 1:1 reference, and the dashed red line indicates the linear fit. Reported values correspond to the fitted slope, r^2, and p-value.

https://doi.org/10.5194/egusphere-2026-4728
Preprint. Discussion started: 8 September 2026
© Author(s) 2026. CC BY 4.0 License.

Appendix B Residual diagnostics

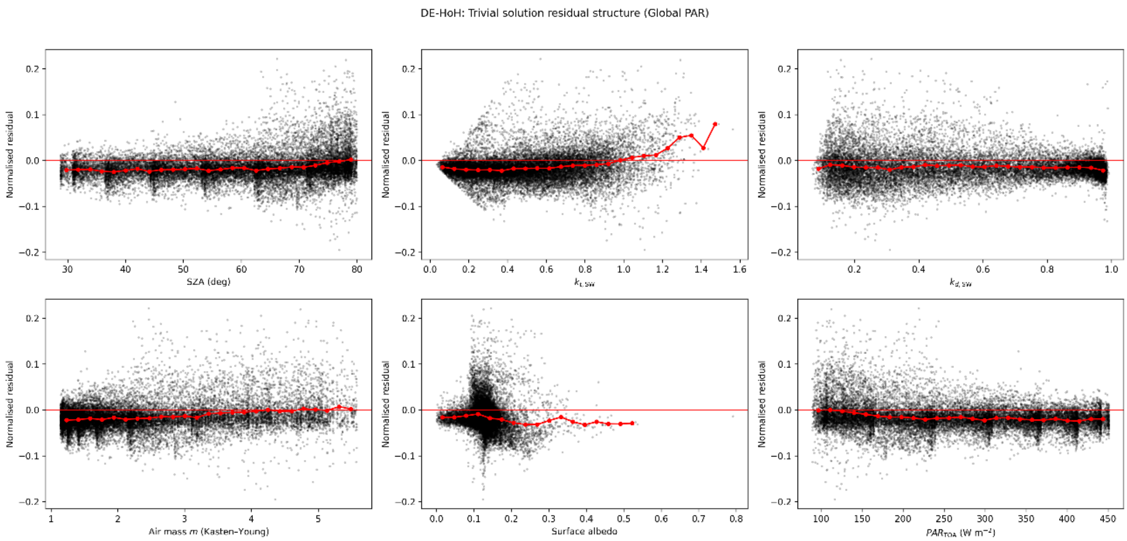

Figure B1. Normalised residual structure of global PAR under the trivial solution for site DE-HoH. Residuals are shown as a function of solar zenith angle (SZA), broadband clearness index $k_{t,SW}$, diffuse fraction $k_{d,SW}$, air mass m, surface albedo, and extraterrestrial PAR irradiance (PAR_{TOA}). Red curves denote bin-averaged trends.

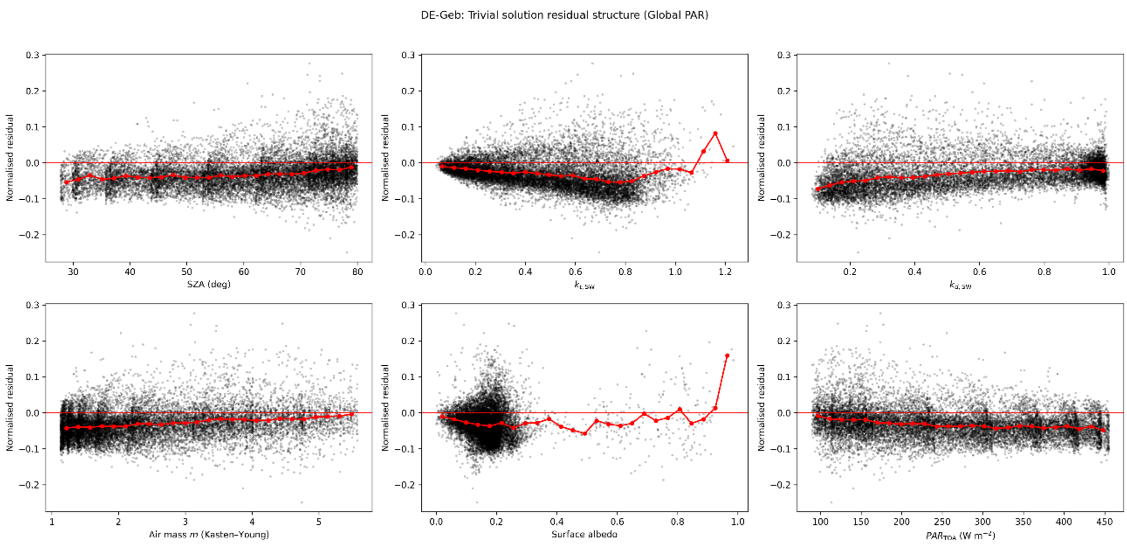

Figure B2. Normalised residual structure of global PAR under the trivial solution for site DE-Geb. Residuals are shown as a function of solar zenith angle (SZA), broadband clearness index $k_{t,SW}$, diffuse fraction $k_{d,SW}$, air mass m, surface albedo, and extraterrestrial PAR irradiance (PAR_{TOA}). Red curves denote bin-averaged trends.

https://doi.org/10.5194/egusphere-2026-4728
Preprint. Discussion started: 8 September 2026
© Author(s) 2026. CC BY 4.0 License.

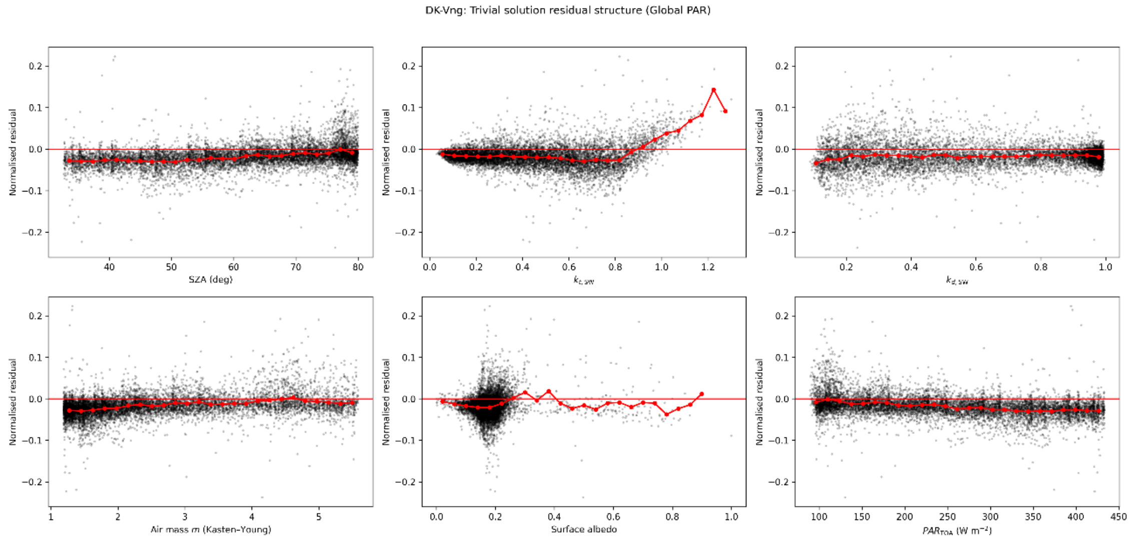

Figure B3. Normalised residual structure of global PAR under the trivial solution for site DK-Vng. Residuals are shown as a function of solar zenith angle (SZA), broadband clearness index $k_{t,SW}$, diffuse fraction $k_{d,SW}$, air mass m, surface albedo, and extraterrestrial PAR irradiance (PAR_{TOA}). Red curves denote bin-averaged trends.

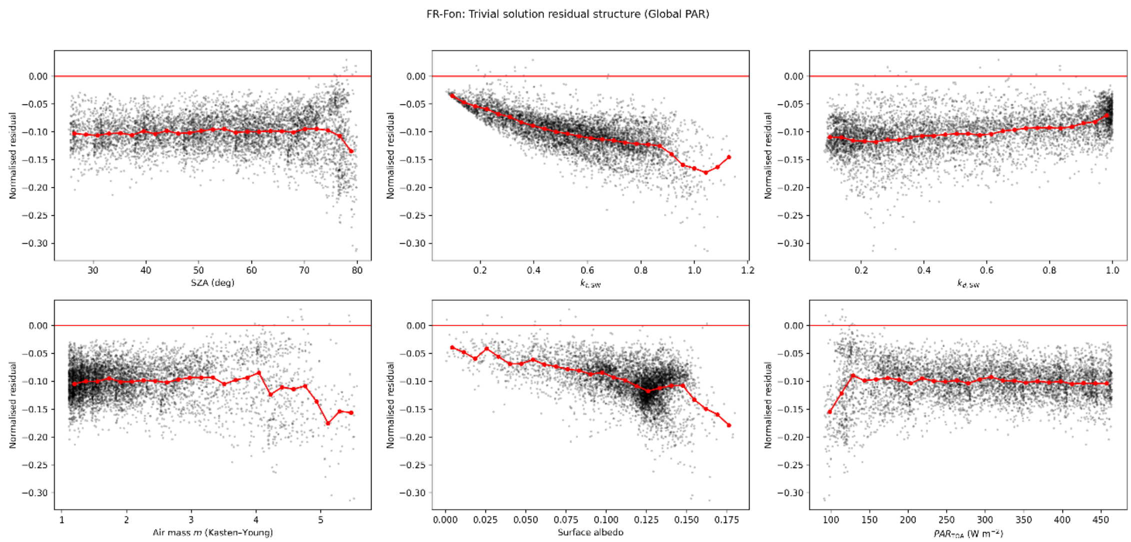

Figure B4. Normalised residual structure of global PAR under the trivial solution for site FR-Fon. Residuals are shown as a function of solar zenith angle (SZA), broadband clearness index $k_{t,SW}$, diffuse fraction $k_{d,SW}$, air mass m, surface albedo, and extraterrestrial PAR irradiance (PAR_{TOA}). Red curves denote bin-averaged trends.

https://doi.org/10.5194/egusphere-2026-4728
Preprint. Discussion started: 8 September 2026
© Author(s) 2026. CC BY 4.0 License.

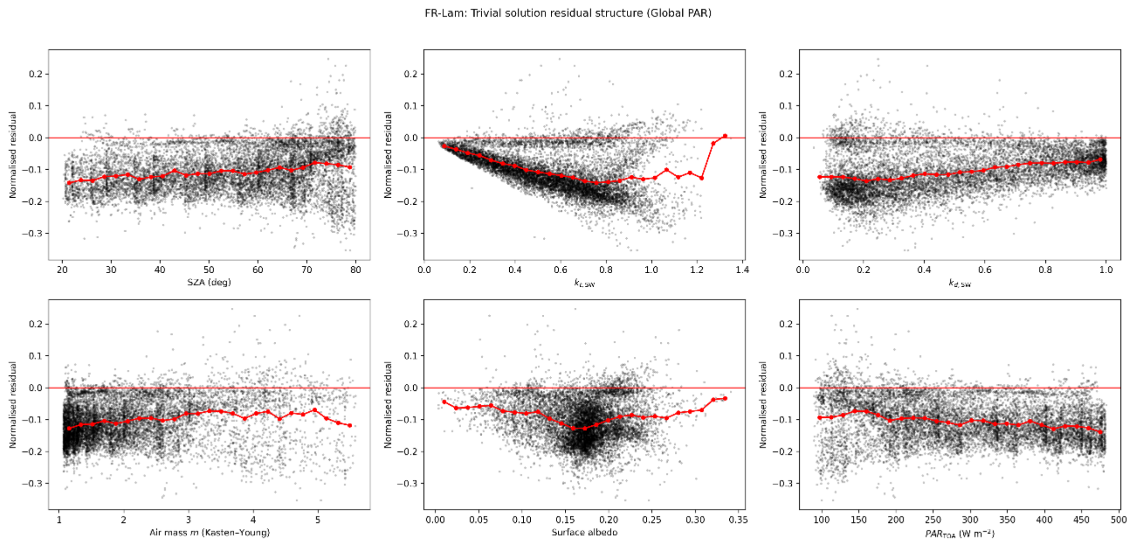

Figure B5. Normalised residual structure of global PAR under the trivial solution for site FR-Lam. Residuals are shown as a function of solar zenith angle (SZA), broadband clearness index $k_{t,SW}$, diffuse fraction $k_{d,SW}$, air mass m, surface albedo, and extraterrestrial PAR irradiance (PAR_{TOA}). Red curves denote bin-averaged trends.

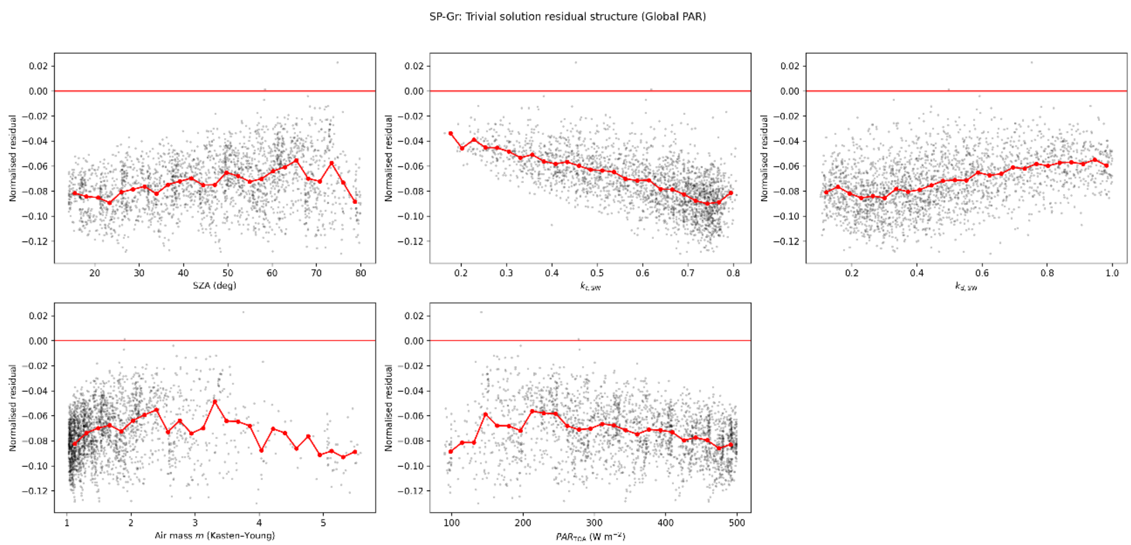

Figure B6. Normalised residual structure of global PAR under the trivial solution for site SP-Gr. Residuals are shown as a function of solar zenith angle (SZA), broadband clearness index $k_{t,SW}$, diffuse fraction $k_{d,SW}$, air mass m, and extraterrestrial PAR irradiance (PAR_{TOA}). Red curves denote bin-averaged trends.

https://doi.org/10.5194/egusphere-2026-4728
Preprint. Discussion started: 8 September 2026
© Author(s) 2026. CC BY 4.0 License.

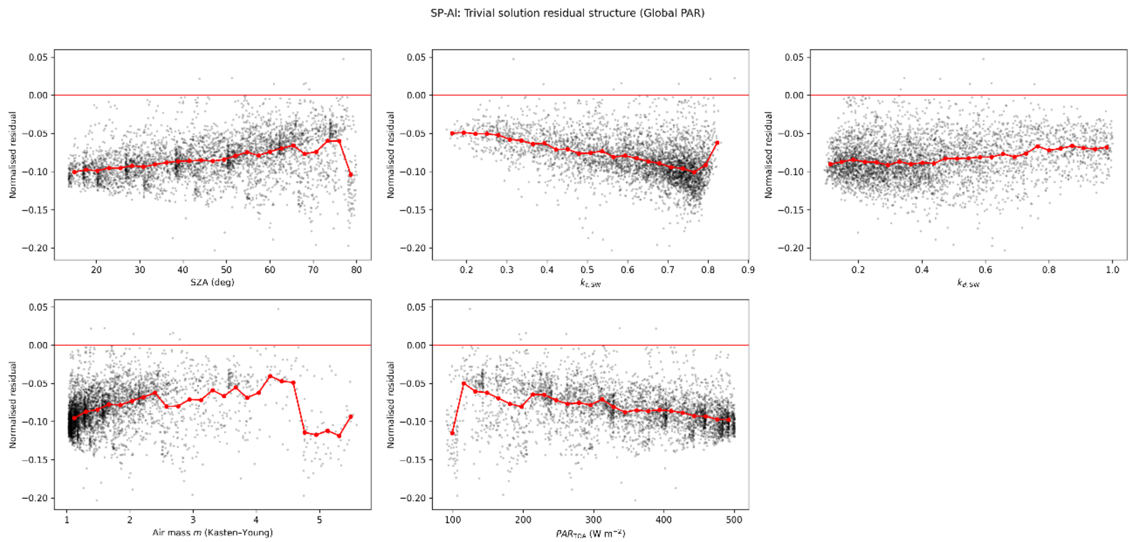

Figure B7. Normalised residual structure of global PAR under the trivial solution for site SP-Al. Residuals are shown as a function of solar zenith angle (SZA), broadband clearness index $k_{t,SW}$, diffuse fraction $k_{d,SW}$, air mass m, and extraterrestrial PAR irradiance (PAR_{TOA}). Red curves denote bin-averaged trends.

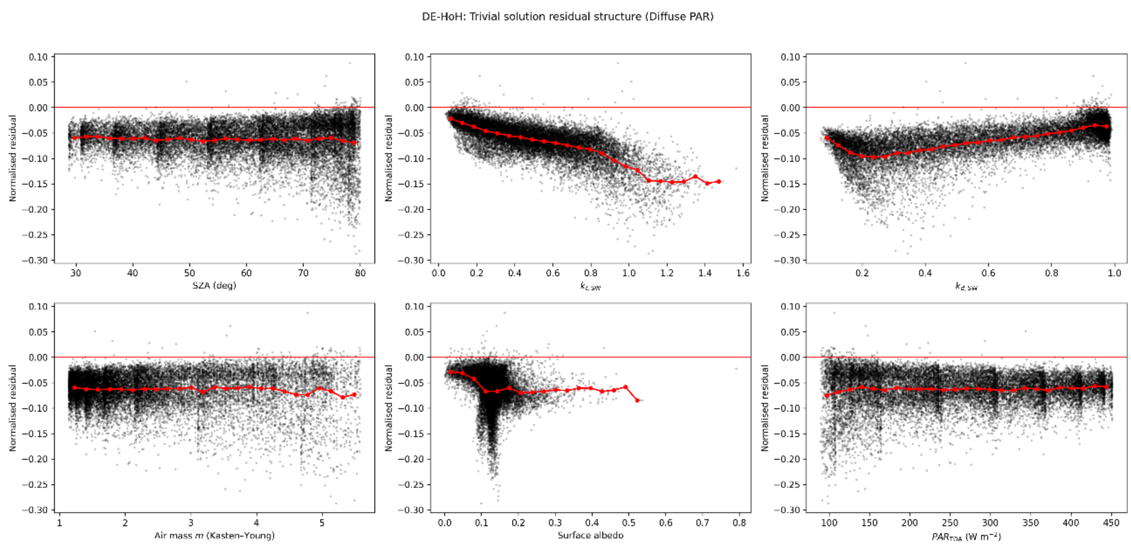

Figure B8. Normalised residual structure of diffuse PAR under the trivial solution for site DE-HoH. Residuals are shown as a function of solar zenith angle (SZA), broadband clearness index $k_{t,SW}$, diffuse fraction $k_{d,SW}$, air mass m, surface albedo, and extraterrestrial PAR irradiance (PAR_{TOA}). Red curves denote bin-averaged trends.

https://doi.org/10.5194/egusphere-2026-4728
Preprint. Discussion started: 8 September 2026
© Author(s) 2026. CC BY 4.0 License.

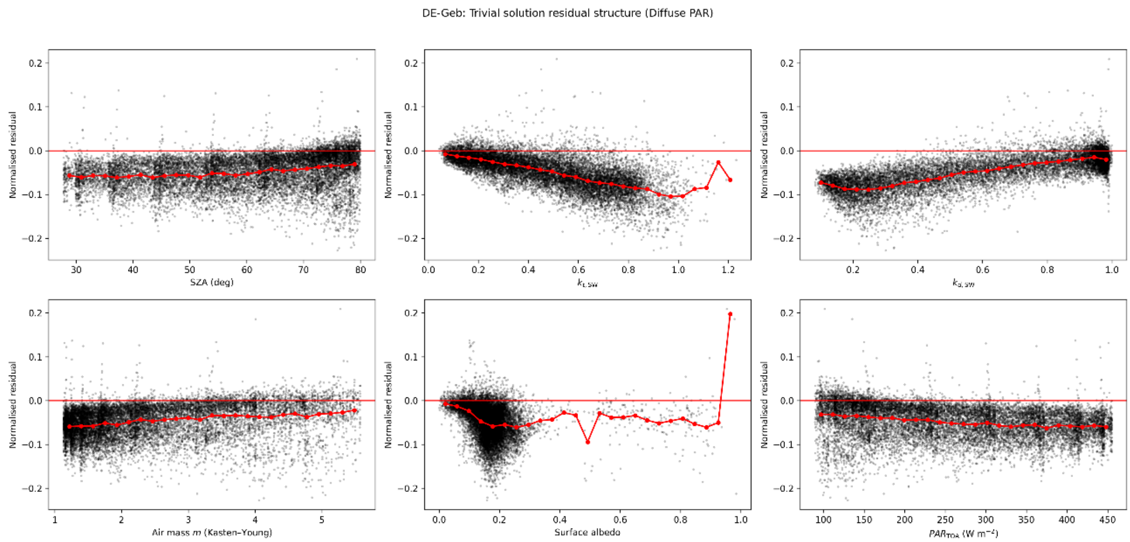

Figure B9. Normalised residual structure of diffuse PAR under the trivial solution for site DE-Geb. Residuals are shown as a function of solar zenith angle (SZA), broadband clearness index $k_{t,SW}$, diffuse fraction $k_{d,SW}$, air mass m, surface albedo, and extraterrestrial PAR irradiance (PAR_{TOA}). Red curves denote bin-averaged trends.

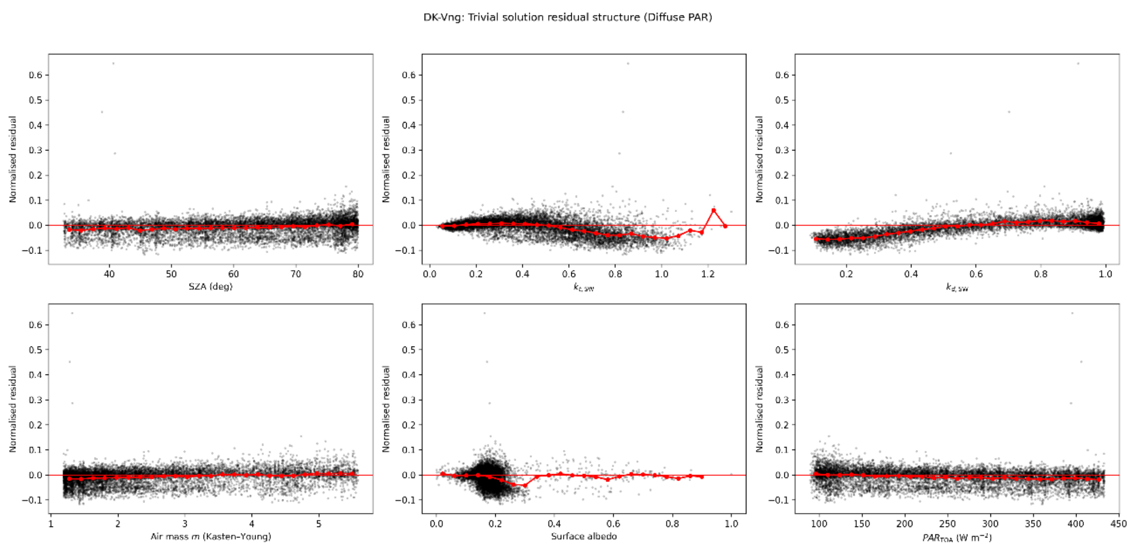

Figure B10. Normalised residual structure of diffuse PAR under the trivial solution for site DK-Vng. Residuals are shown as a function of solar zenith angle (SZA), broadband clearness index $k_{t,SW}$, diffuse fraction $k_{d,SW}$, air mass m, surface albedo, and extraterrestrial PAR irradiance (PAR_{TOA}). Red curves denote bin-averaged trends.

https://doi.org/10.5194/egusphere-2026-4728
Preprint. Discussion started: 8 September 2026
© Author(s) 2026. CC BY 4.0 License.

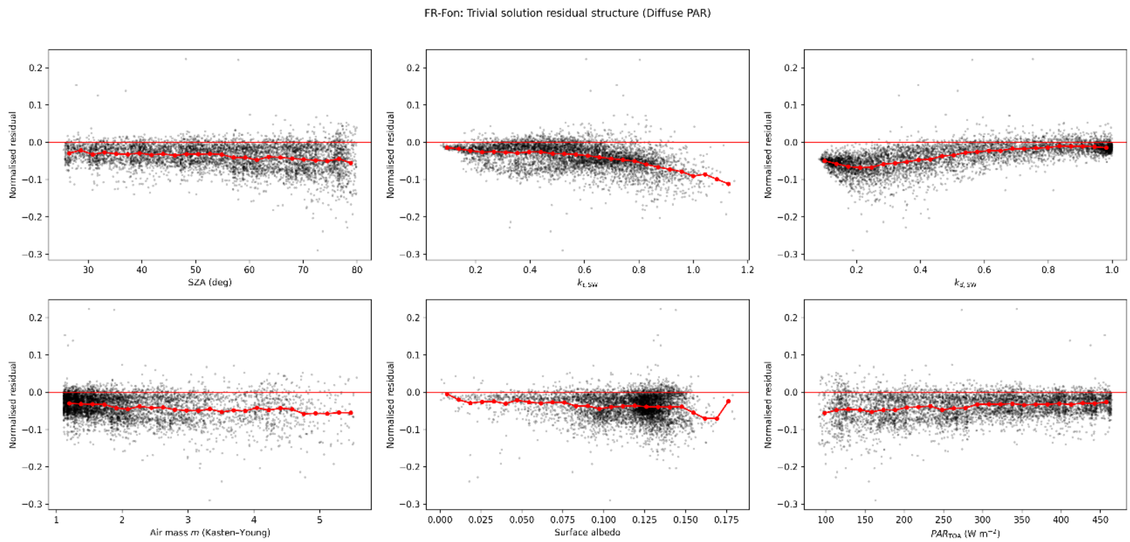

Figure B11. Normalised residual structure of diffuse PAR under the trivial solution for site FR-Fon. Residuals are shown as a function of solar zenith angle (SZA), broadband clearness index $k_{t,SW}$, diffuse fraction $k_{d,SW}$, air mass m, surface albedo, and extraterrestrial PAR irradiance (PAR_{TOA}). Red curves denote bin-averaged trends.

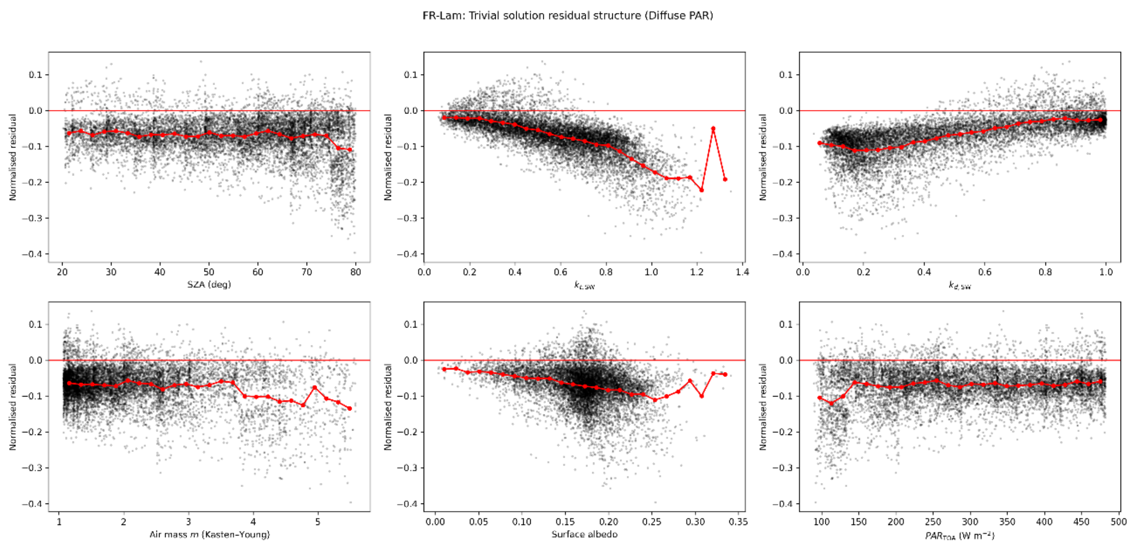

Figure B12. Normalised residual structure of diffuse PAR under the trivial solution for site FR-Lam. Residuals are shown as a function of solar zenith angle (SZA), broadband clearness index $k_{t,SW}$, diffuse fraction $k_{d,SW}$, air mass m, surface albedo, and extraterrestrial PAR irradiance (PAR_{TOA}). Red curves denote bin-averaged trends.

https://doi.org/10.5194/egusphere-2026-4728
Preprint. Discussion started: 8 September 2026
© Author(s) 2026. CC BY 4.0 License.

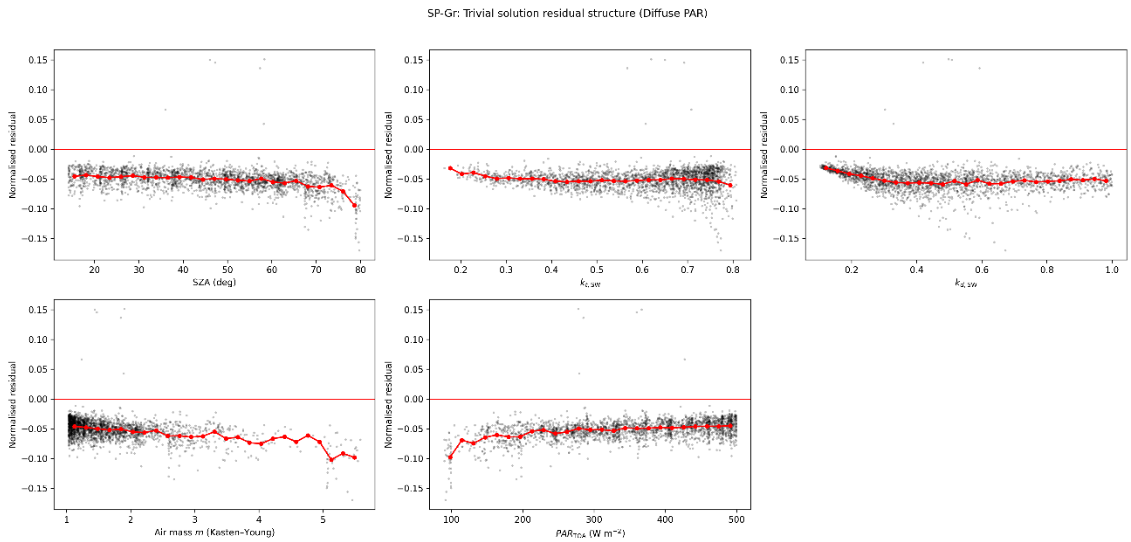

Figure B13. Normalised residual structure of diffuse PAR under the trivial solution for site SP-Gr. Residuals are shown as a function of solar zenith angle (SZA), broadband clearness index $k_{t,SW}$, diffuse fraction $k_{d,SW}$, air mass m, and extraterrestrial PAR irradiance (PAR_{TOA}). Red curves denote bin-averaged trends.

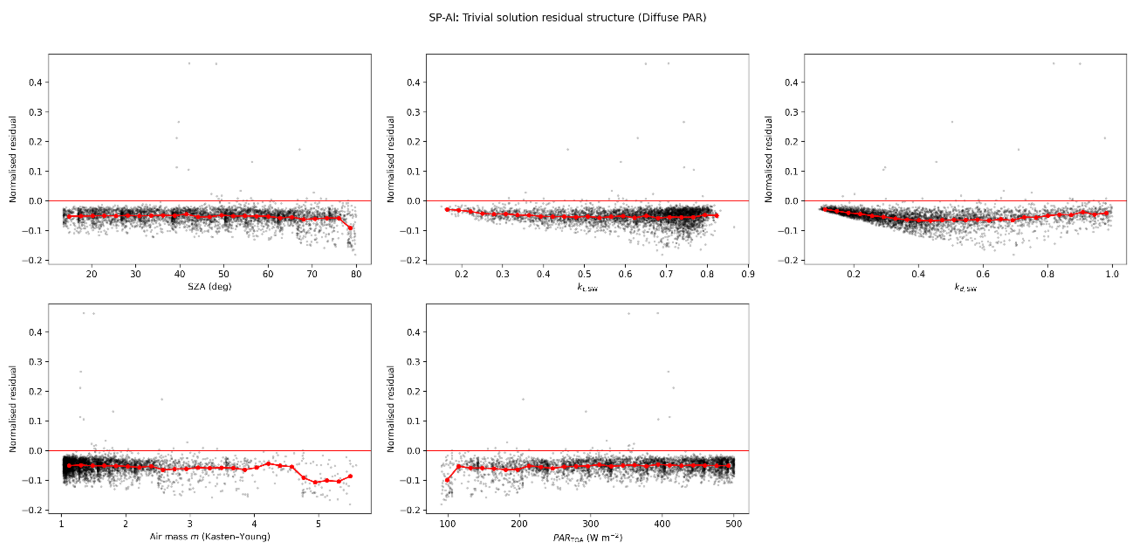

Figure B14. Normalised residual structure of diffuse PAR under the trivial solution for site SP-Al. Residuals are shown as a function of solar zenith angle (SZA), broadband clearness index $k_{t,SW}$, diffuse fraction $k_{d,SW}$, air mass m, and extraterrestrial PAR irradiance (PAR_{TOA}). Red curves denote bin-averaged trends.

https://doi.org/10.5194/egusphere-2026-4728
Preprint. Discussion started: 8 September 2026
© Author(s) 2026. CC BY 4.0 License.

Code and data availability

The Spanish radiometric datasets from Granada (1994–1995) and Almería (1993–1995), including simultaneous measurements of global and diffuse photosynthetically active radiation (PAR) and broadband shortwave radiation, are available from the corresponding author upon reasonable request.

The ICOS ecosystem station meteorological datasets used in this study are publicly available through the ICOS Carbon Portal (https://www.icos-cp.eu) and correspond to quality-controlled ETC NRT or L2 Meteo products. The specific datasets used are: DE-Geb (Brümmer et al., 2026), DE-HoH (Rebmann et al., 2025), DK-Vng (Friborg et al., 2024), FR-Fon (Berveiller et al., 2026), and FR-Lam (Brut et al., 2025). All ICOS data were accessed in accordance with the ICOS data policy.

All data processing and analysis were performed using Python (version 3.13). Core libraries included NumPy, Pandas, SciPy, and Matplotlib for numerical computation, statistical analysis, and visualisation.

Author contributions

I.L.L. conceived the study, developed the methodology and theoretical framework, implemented the software and data processing, performed the formal analysis and validation, prepared the visualizations, and wrote the original manuscript draft. E.E., I.F.-M., I.A., and M.K. contributed through scientific discussion, interpretation of results, and critical review and editing of the manuscript. All authors reviewed and approved the final version of the manuscript.

Competing interests

The authors declare that they have no conflict of interest.

Acknowledgements

Open access funding provided by the University of Helsinki. I.L.L. acknowledges the Holistic infrastructure for knowledge on land-use sector carbon sinks and emissions tracking (HIKET) project for institutional support.

Financial support

This research has not received any specific grant from funding agencies in the public, commercial, or not-for-profit sectors.

References

Alados, I. and Alados-Arboledas, L.: Direct and diffuse photosynthetically active radiation: measurements and modelling, Agricultural and Forest Meteorology, 93, 27–38, https://doi.org/10.1016/S0168-1923(98)00107-5, 1999a.

https://doi.org/10.5194/egusphere-2026-4728
Preprint. Discussion started: 8 September 2026
© Author(s) 2026. CC BY 4.0 License.

Alados, I. and Alados-Arboledas, L.: Validation of an empirical model for photosynthetically active radiation, Int. J. Climatol., 19, 1145–1152, https://doi.org/10.1002/(SICI)1097-0088(199908)19:10%3C1145::AID-JOC428%3E3.0.CO;2-3, 1999b.

Alados, I., Foyo-Moreno, I., Olmo, F. J., and Alados-Arboledas, L.: Improved estimation of diffuse photosynthetically active radiation using two spectral models, Agricultural and Forest Meteorology, 111, 1–12, https://doi.org/10.1016/S0168-1923(02)00010-2, 2002.

Ångström, A.: The parameters of atmospheric turbidity, Tellus, 16, 64–75, https://doi.org/10.3402/tellusa.v16i1.8885, 1964.

Baldocchi, D., Falge, E., Gu, L., Olson, R., Hollinger, D., Running, S., Anthoni, P., Bernhofer, C., Davis, K., Evans, R., Fuentes, J., Goldstein, A., Katul, G., Law, B., Lee, X., Malhi, Y., Meyers, T., Munger, W., Oechel, W., U, K. T. P., Pilegaard, K., Schmid, H. P., Valentini, R., Verma, S., Vesala, T., Wilson, K., and Wofsy, S.: FLUXNET: A New Tool to Study the Temporal and Spatial Variability of Ecosystem-Scale Carbon Dioxide, Water Vapor, and Energy Flux Densities, Bulletin of the American Meteorological Society, 82, 2415–2434, https://doi.org/10.1175/1520-0477(2001)082%3C2415:FANTTS%3E2.3.CO;2, 2001.

Barnard, J. C. and Long, C. N.: A Simple Empirical Equation to Calculate Cloud Optical Thickness Using Shortwave Broadband Measurements, Journal of Applied Meteorology and Climatology, 43, 1057–1066, https://doi.org/10.1175/1520-0450(2004)043%3C1057:ASEETC%3E2.0.CO;2, 2004.

Barnes, P. W., Robson, T. M., Zepp, R. G., Bornman, J. F., Jansen, M. A. K., Ossola, R., Wang, Q.-W., Robinson, S. A., Foereid, B., Klekociuk, A. R., Martinez-Abaigar, J., Hou, W.-C., Mackenzie, R., and Paul, N. D.: Interactive effects of changes in UV radiation and climate on terrestrial ecosystems, biogeochemical cycles, and feedbacks to the climate system, Photochem Photobiol Sci, 22, 1049–1091, https://doi.org/10.1007/s43630-023-00376-7, 2023.

Batlles, F. J., Olmo, F. J., and Alados-Arboledas, L.: On shadowband correction methods for diffuse irradiance measurements, Solar Energy, 54, 105–114, https://doi.org/10.1016/0038-092X(94)00115-T, 1995.

Berveiller, D., Dufrêne, E., Delpierre, N., Morfin, A., Francois, C., Vincent, G., Bazot, S., Soudani, K., Girardin, C., Guillot, T., and Perot-Guillaume, C.: ETC L2 Meteo from Fontainebleau-Barbeau | ICOS, 2025.

Bird, R. E. and Hulstrom, R. L.: Simplified clear sky model for direct and diffuse insolation on horizontal surfaces, Solar Energy Research Inst., Golden, CO (USA), https://doi.org/10.2172/6510849, 1981.

Bird, R. E. and Riordan, C.: Simple solar spectral model for direct and diffuse irradiance on horizontal and tilted planes at the earth's surface for cloudless atmospheres, Journal of climate and applied meteorology, 25, 87–97, 1986.

Bohren, C. F.: Fundamentals of atmospheric radiation: an introduction with 400 problems, Wiley-VCH, Weinheim, 492 pp., 2006.

Bonan, G.: Climate Change and Terrestrial Ecosystem Modeling, Cambridge University Press, Cambridge, https://doi.org/10.1017/9781107339217, 2019.

Brümmer, C., Akubia, J., Delorme, J., Schrader, F., and Shivhalli Gopal, A.: ETC L2 Meteo from Gebesee | ICOS, 2025.

Brut, A., Tallec, T., Granouillac, F., Zawilski, B., Claverie, N., Lemaire, B., and Ceschia, E.: ETC L2 Meteo from Lamasquere | ICOS, 2025.

https://doi.org/10.5194/egusphere-2026-4728
Preprint. Discussion started: 8 September 2026
© Author(s) 2026. CC BY 4.0 License.

Carrara, A., Kolari, P., Beeck, M. O. de, Arriga, N., Berveiller, D., Dengel, S., Ibrom, A., Merbold, L., Rebmann, C., Sabbatini, S., Serrano-Ortiz, P., and Biraud, S. C.: Radiation measurements at ICOS ecosystem stations, Int. Agrophys., 32, 589–605, https://doi.org/10.1515/intag-2017-0049, 2018.

Chakrabarty, R. K., Shetty, N. J., Thind, A. S., Beeler, P., Sumlin, B. J., Zhang, C., Liu, P., Idrobo, J. C., Adachi, K., Wagner, N. L., Schwarz, J. P., Ahern, A., Sedlacek, A. J., Lambe, A., Daube, C., Lyu, M., Liu, C., Herndon, S., Onasch, T. B., and Mishra, R.: Shortwave absorption by wildfire smoke dominated by dark brown carbon, Nat. Geosci., 16, 683–688, https://doi.org/10.1038/s41561-023-01237-9, 2023.

Chandrasekhar, S.: Radiative Transfer, Courier Corporation, 418 pp., 2013.

Chen, C., Dubovik, O., Schuster, G. L., Chin, M., Henze, D. K., Lapyonok, T., Li, Z., Derimian, Y., and Zhang, Y.: Multi-angular polarimetric remote sensing to pinpoint global aerosol absorption and direct radiative forcing, Nat Commun, 13, 7459, https://doi.org/10.1038/s41467-022-35147-y, 2022.

Emery, W. and Camps, A.: Introduction to Satellite Remote Sensing: Atmosphere, Ocean, Cryosphere and Land Applications, Elsevier, https://doi.org/10.1016/C2015-0-04517-8, 2017.

Erbs, D. G., Klein, S. A., and Duffie, J. A.: Estimation of the diffuse radiation fraction for hourly, daily and monthly-average global radiation, Solar Energy, 28, 293–302, https://doi.org/10.1016/0038-092X(82)90302-4, 1982.

Ferrera-Cobos, F., Vindel, J. M., Valenzuela, R. X., and González, J. A.: Models for estimating daily photosynthetically active radiation in oceanic and mediterranean climates and their improvement by site adaptation techniques, Advances in Space Research, 65, 1894–1909, https://doi.org/10.1016/j.asr.2020.01.018, 2020.

Foyo-Moreno, I., Alados, I., and Alados-Arboledas, L.: A new conventional regression model to estimate hourly photosynthetic photon flux density under all sky conditions, International Journal of Climatology, 37, 1067–1075, https://doi.org/10.1002/joc.5063, 2017.

Foyo-Moreno, I., Alados, I., and Alados-Arboledas, L.: A new empirical model to estimate hourly diffuse photosynthetic photon flux density, Atmospheric Research, 203, 189–196, https://doi.org/10.1016/j.atmosres.2017.12.012, 2018.

Friborg, T., Jensen, R., and Rasmussen, L.: ETC L2 Meteo from Voulundgaard | ICOS, 2024.

García-Rodríguez, A., Granados-López, D., García-Rodríguez, S., Díez-Mediavilla, M., and Alonso-Tristán, C.: Modelling Photosynthetic Active Radiation (PAR) through meteorological indices under all sky conditions, Agricultural and Forest Meteorology, 310, 108627, https://doi.org/10.1016/j.agrformet.2021.108627, 2021.

García-Rodríguez, A., García-Rodríguez, S., Granados-López, D., Díez-Mediavilla, M., and Alonso-Tristán, C.: Extension of PAR Models under Local All-Sky Conditions to Different Climatic Zones, Applied Sciences, 12, 2372, https://doi.org/10.3390/app12052372, 2022.

Gu, L. H., Baldocchi, D., Verma, S. B., Black, T. A., Vesala, T., Falge, E. M., and Dowty, P. R.: Advantages of diffuse radiation for terrestrial ecosystem productivity, J. Geophys. Res.-Atmos., 107, 4050, https://doi.org/10.1029/2001JD001242, 2002.

Gueymard, C. A.: A two-band model for the calculation of clear sky solar irradiance, illuminance, and photosynthetically active radiation at the earth’s surface, Solar Energy, 43, 253–265, https://doi.org/10.1016/0038-092X(89)90113-8, 1989.

https://doi.org/10.5194/egusphere-2026-4728
Preprint. Discussion started: 8 September 2026
© Author(s) 2026. CC BY 4.0 License.

Gueymard, C. A.: Direct solar transmittance and irradiance predictions with broadband models. Part I: detailed theoretical performance assessment, Solar Energy, 74, 355–379, https://doi.org/10.1016/S0038-092X(03)00195-6, 2003.

Gueymard, C. A.: The sun's total and spectral irradiance for solar energy applications and solar radiation models, Solar Energy, 76, 423–453, https://doi.org/10.1016/j.solener.2003.08.039, 2004.

Gueymard, C. A.: Clear-sky irradiance predictions for solar resource mapping and large-scale applications: Improved validation methodology and detailed performance analysis of 18 broadband radiative models, Solar Energy, 86, 2145–2169, https://doi.org/10.1016/j.solener.2011.11.011, 2012.

Gueymard, C. A.: Revised composite extraterrestrial spectrum based on recent solar irradiance observations, Solar Energy, 169, 434–440, https://doi.org/10.1016/j.solener.2018.04.067, 2018.

Hu, Y. X. and Stamnes, K.: An Accurate Parameterization of the Radiative Properties of Water Clouds Suitable for Use in Climate Models, Journal of Climate, 6, 728–742, 1993.

Iqbal, M.: An Introduction to Solar-Radiation, Bull. Amer. Meteorol. Soc., 65, 1113–1113, 1983.

Janjai, S. and Wattan, R.: Development of a model for the estimation of photosynthetically active radiation from geostationary satellite data in a tropical environment, Remote Sensing of Environment, 115, 1680–1693, https://doi.org/10.1016/j.rse.2011.02.026, 2011.

Jung, Y., Lee, H., Kim, J., Cho, Y., Kim, J., and Lee, Y. G.: Spatio-Temporal Characteristics in the Clearness Index Derived from Global Solar Radiation Observations in Korea, Atmosphere, 7, https://doi.org/10.3390/atmos7040055, 2016.

Kasten, F. and Young, A. T.: Revised optical air mass tables and approximation formula, Applied Optics, Vol. 28, Issue 22, pp. 4735-4738, https://doi.org/10.1364/AO.28.004735, 1989.

Kato, S., Ackerman, T. P., Mather, J. H., and Clothiaux, E. E.: The k-distribution method and correlated-k approximation for a shortwave radiative transfer model, Journal of Quantitative Spectroscopy and Radiative Transfer, 62, 109–121, https://doi.org/10.1016/S0022-4073(98)00075-2, 1999.

Kikuchi, N., Nakajima, T., Kumagai, H., Kuroiwa, H., Kamei, A., Nakamura, R., and Nakajima, T. Y.: Cloud optical thickness and effective particle radius derived from transmitted solar radiation measurements: Comparison with cloud radar observations, Journal of Geophysical Research: Atmospheres, 111, https://doi.org/10.1029/2005JD006363, 2006.

Kim, J., Lee, Y. G., Koo, J.-H., and Lee, H.: Relative Contributions of Clouds and Aerosols to Surface Erythemal UV and Global Horizontal Irradiance in Korea, Energies, 13, https://doi.org/10.3390/en13061504, 2020.

Kokhanovsky, A. A.: Cloud Optics, Springer Netherlands, Dordrecht, https://doi.org/10.1007/1-4020-4020-2, 2006.

Lawrence, D. M., Fisher, R. A., Koven, C. D., Oleson, K. W., Swenson, S. C., Bonan, G., Collier, N., Ghimire, B., van Kampenhout, L., Kennedy, D., Kluzek, E., Lawrence, P. J., Li, F., Li, H., Lombardozzi, D., Riley, W. J., Sacks, W. J., Shi, M., Vertenstein, M., Wieder, W. R., Xu, C., Ali, A. A., Badger, A. M., Bisht, G., van den Broeke, M., Brunke, M. A., Burns, S. P., Buzan, J., Clark, M., Craig, A., Dahlin, K., Drewniak, B., Fisher, J. B., Flanner, M., Fox, A. M., Gentine, P., Hoffman, F., Keppel-Aleks, G., Knox, R., Kumar, S., Lenaerts, J., Leung, L. R., Lipscomb, W. H., Lu, Y., Pandey, A., Pelletier, J. D., Perket, J., Randerson, J. T., Ricciuto, D. M., Sanderson, B. M., Slater, A., Subin, Z. M., Tang, J., Thomas, R. Q., Val Martin, M., and Zeng, X.: The Community Land Model Version 5: Description of New Features, Benchmarking, and Impact of Forcing Uncertainty, Journal of Advances in Modeling Earth Systems, 11, 4245–4287, https://doi.org/10.1029/2018MS001583, 2019.

https://doi.org/10.5194/egusphere-2026-4728
Preprint. Discussion started: 8 September 2026
© Author(s) 2026. CC BY 4.0 License.

Liou, K. N.: An Introduction to Atmospheric Radiation, Academic Press, 599 pp., 2002.

Lozano, I. L., Sánchez-Hernández, G., Guerrero-Rascado, J. L., Alados, I., and Foyo-Moreno, I.: Aerosol radiative effects in photosynthetically active radiation and total irradiance at a Mediterranean site from an 11-year database, Atmospheric Research, 255, 105538, https://doi.org/10.1016/j.atmosres.2021.105538, 2021.

Lozano, I. L., Sánchez-Hernández, G., Guerrero-Rascado, J. L., Alados, I., and Foyo-Moreno, I.: Analysis of cloud effects on long-term global and diffuse photosynthetically active radiation at a Mediterranean site, Atmospheric Research, 268, 106010, https://doi.org/10.1016/j.atmosres.2021.106010, 2022.

Lozano, I. L., Alados, I., Sánchez-Hernández, G., Guerrero-Rascado, J. L., and Foyo-Moreno, I.: Improving the Estimation of the Diffuse Component of Photosynthetically Active Radiation (PAR), Journal of Geophysical Research: Atmospheres, 128, e2023JD039256, https://doi.org/10.1029/2023JD039256, 2023.

Ma Lu, S., Yang, D., Anderson, M. C., Zainali, S., Stridh, B., Avelin, A., and Campana, P. E.: Photosynthetically active radiation separation model for high-latitude regions in agrivoltaic systems modeling, J. Renewable Sustainable Energy, 16, 013503, https://doi.org/10.1063/5.0181311, 2024.

McCree, K. J.: Test of current definitions of photosynthetically active radiation against leaf photosynthesis data, Agricultural Meteorology, 10, 443–453, https://doi.org/10.1016/0002-1571(72)90045-3, 1972.

Mercado, L. M., Bellouin, N., Sitch, S., Boucher, O., Huntingford, C., Wild, M., and Cox, P. M.: Impact of changes in diffuse radiation on the global land carbon sink, Nature, 458, 1014–1017, https://doi.org/10.1038/nature07949, 2009.

Meyer, K., Yang, P., and Gao, B.-C.: Optical thickness of tropical cirrus clouds derived from the MODIS 0.66and 1.375-/spl mu/m channels, IEEE Transactions on Geoscience and Remote Sensing, 42, 833–841, https://doi.org/10.1109/TGRS.2003.818939, 2004.

Myhre, G., Shindell, D., Bréon, F. M., Collins, W., Fuglestvedt, J., Huang, J., Koch, D., Lamarque, J. F., Lee, D., Mendoza, B., Nakajima, T., Robock, A., Stephens, G., Takemura, T., and Zhang, H.: Anthropogenic and Natural Radiative Forcing, in: Climate Change 2013 - The Physical Science Basis, edited by: Change, I. P. on C., Cambridge University Press, Cambridge, 659–740, https://doi.org/10.1017/CBO9781107415324.018, 2013.

Nemitz, E., Mammarella, I., Ibrom, A., Aurela, M., Burba, G. G., Dengel, S., Gielen, B., Grelle, A., Heinesch, B., Herbst, M., Hörtnagl, L., Klemedtsson, L., Lindroth, A., Lohila, A., McDermitt, D. K., Meier, P., Merbold, L., Nelson, D., Nicolini, G., Nilsson, M. B., Peltola, O., Rinne, J., and Zahniser, M.: Standardisation of eddy-covariance flux measurements of methane and nitrous oxide, Int. Agrophys., 32, 517–549, https://doi.org/10.1515/intag-2017-0042, 2018.

Noll, S., Kausch, W., Barden, M., Jones, A. M., Szyszka, C., Kimeswenger, S., and Vinther, J.: An atmospheric radiation model for Cerro Paranal - I. The optical spectral range, A&A, 543, A92, https://doi.org/10.1051/0004-6361/201219040, 2012.

Pastorello, G., Trotta, C., Canfora, E., Chu, H., Christianson, D., Cheah, Y.-W., Poindexter, C., Chen, J., Elbashandy, A., Humphrey, M., Isaac, P., Polidori, D., Reichstein, M., Ribeca, A., van Ingen, C., Vuichard, N., Zhang, L., Amiro, B., Ammann, C., Arain, M. A., Ardö, J., Arkebauer, T., Arndt, S. K., Arriga, N., Aubinet, M., Aurela, M., Baldocchi, D., Barr, A., Beamesderfer, E., Marchesini, L. B., Bergeron, O., Beringer, J., Bernhofer, C., Berveiller, D., Billesbach, D., Black, T. A., Blanken, P. D., Bohrer, G., Boike, J., Bolstad, P. V., Bonal, D., Bonnefond, J.-M., Bowling, D. R., Bracho, R., Brodeur, J., Brümmer, C., Buchmann, N., Burban, B., Burns, S. P., Buysse, P., Cale, P., Cavagna, M., Cellier, P., Chen, S., Chini, I., Christensen, T. R., Cleverly, J., Collalti, A., Consalvo, C., Cook, B. D., Cook, D., Coursolle, C., Cremonese, E., Curtis, P. S., D'Andrea, E., da Rocha, H., Dai, X., Davis, K. J., Cinti, B. D., Grandcourt, A. de, Ligne, A. D., De Oliveira, R. C., Delpierre, N., Desai, A. R., Di Bella, C. M., Tommasi, P. di, Dolman, H., Domingo, F., Dong, G., Dore, S., Duce, P., Dufrêne, E., Dunn,

https://doi.org/10.5194/egusphere-2026-4728
Preprint. Discussion started: 8 September 2026
© Author(s) 2026. CC BY 4.0 License.

A., Dušek, J., Eamus, D., Eichelmann, U., ElKhidir, H. A. M., Eugster, W., Ewenz, C. M., Ewers, B., Famulari, D., Fares, S., Feigenwinter, I., Feitz, A., Fensholt, R., Filippa, G., Fischer, M., Frank, J., Galvagno, M., et al.: The FLUXNET2015 dataset and the ONEFlux processing pipeline for eddy covariance data, Sci Data, 7, 225, https://doi.org/10.1038/s41597-020-0534-3, 2020.

Ramanathan, V., Cess, R. D., Harrison, E. F., Minnis, P., Barkstrom, B. R., Ahmad, E., and Hartmann, D.: Cloud-Radiative Forcing and Climate: Results from the Earth Radiation Budget Experiment, Science, 243, 57–63, https://doi.org/10.1126/science.243.4887.57, 1989.

Ramanathan, V., Crutzen, P. J., Kiehl, J. T., and Rosenfeld, D.: Aerosols, Climate, and the Hydrological Cycle, Science, 294, 2119–2124, https://doi.org/10.1126/science.1064034, 2001.

Rebmann, C., Dienstbach, L., Schmidt, P., Wiesen, R., Meis, J., Feldmann, I., Bastos Campos, F., Dejosez, S., Garcia Quiros, I., Gimper, S., Hautmann, D., Hildebrandt, A., Kempka, P., and Paasch, S.: ETC L2 Meteo from Hohes Holz | ICOS, 2025.

Reindl, D. T., Beckman, W. A., and Duffie, J. A.: Diffuse fraction correlations, Solar Energy, 45, 1–7, https://doi.org/10.1016/0038-092X(90)90060-P, 1990.

Slingo, A.: A GCM Parameterization for the Shortwave Radiative Properties of Water Clouds, Journal of the Atmospheric Sciences, 46, 1419–1427, https://doi.org/10.1175/1520-0469(1989)046%3C1419:AGPFTS%3E2.0.CO;2, 1989.

Stamnes, K., Thomas, G. E., and Stamnes, J. J.: Radiative Transfer in the Atmosphere and Ocean, 2nd ed., Cambridge University Press, Cambridge, https://doi.org/10.1017/9781316148549, 2017.

Stephens, G. L.: Radiation Profiles in Extended Water Clouds. II: Parameterization Schemes, Journal of the Atmospheric Sciences, 35, 2123–2132, https://doi.org/10.1175/1520-0469(1978)035%3C2123:RPIEWC%3E2.0.CO;2, 1978.

Thornhill, G. D., Collins, W. J., Kramer, R. J., Olivié, D., O'Connor, F., Abraham, N. L., Bauer, S. E., Deushi, M., Emmons, L., Forster, P., Horowitz, L., Johnson, B., Keeble, J., Lamarque, J.-F., Michou, M., Mills, M., Mulcahy, J., Myhre, G., Nabat, P., Naik, V., Oshima, N., Schulz, M., Smith, C., Takemura, T., Tilmes, S., Wu, T., Zeng, G., and Zhang, J.: Effective Radiative forcing from emissions of reactive gases and aerosols – a multimodel comparison, Aerosols/Atmospheric Modelling/Troposphere/Physics (physical properties and processes), https://doi.org/10.5194/acp-2019-1205, 2020.

Van Laake, P. E. and Sanchez-Azofeifa, G. A.: Simplified atmospheric radiative transfer modelling for estimating incident PAR using MODIS atmosphere products, Remote Sensing of Environment, 91, 98–113, https://doi.org/10.1016/j.rse.2004.03.002, 2004.

Van Laake, P. E. and Sanchez-Azofeifa, G. A.: Mapping PAR using MODIS atmosphere products, Remote Sensing of Environment, 94, 554–563, https://doi.org/10.1016/j.rse.2004.11.011, 2005.

Vindel, J. M., Valenzuela, R. X., Navarro, A. A., Zarzalejo, L. F., Paz-Gallardo, A., Souto, J. A., Méndez-Gómez, R., Cartelle, D., and Casares, J. J.: Modeling Photosynthetically Active Radiation from Satellite-Derived Estimations over Mainland Spain, Remote Sensing, 10, 849, https://doi.org/10.3390/rs10060849, 2018.

Wen, G., Marshak, A., and Cahalan, R. F.: Importance of molecular Rayleigh scattering in the enhancement of clear sky reflectance in the vicinity of boundary layer cumulus clouds, Journal of Geophysical Research: Atmospheres, 113, https://doi.org/10.1029/2008JD010592, 2008.

Wild, M.: Enlightening Global Dimming and Brightening, Bulletin of the American Meteorological Society, 93, 27–37, https://doi.org/10.1175/BAMS-D-11-00074.1, 2012.

https://doi.org/10.5194/egusphere-2026-4728
Preprint. Discussion started: 8 September 2026
© Author(s) 2026. CC BY 4.0 License.

Wild, M.: Decadal changes in radiative fluxes at land and ocean surfaces and their relevance for global warming, Wiley Interdiscip. Rev.-Clim. Chang., 7, 91–107, https://doi.org/10.1002/wcc.372, 2016.

Wild, M., Wacker, S., Yang, S., and Sanchez-Lorenzo, A.: Evidence for Clear-Sky Dimming and Brightening in Central Europe, Geophysical Research Letters, 48, e2020GL092216, https://doi.org/10.1029/2020GL092216, 2021.

Wild, M., Wang, Y., Wang, K., and Yang, S.: A Perspective on Global Dimming and Brightening Worldwide and in China, Adv. Atmos. Sci., 43, 281–294, https://doi.org/10.1007/s00376-025-4534-2, 2026.

Ylivinkka, I., Kaupinmäki, S., Virman, M., Peltola, M., Taipale, D., Petäjä, T., Kerminen, V.-M., Kulmala, M., and Ezhova, E.: Clouds over Hyytiälä, Finland: an algorithm to classify clouds based on solar radiation and cloud base height measurements, Atmospheric Measurement Techniques, 13, 5595–5619, https://doi.org/10.5194/amt-13-5595-2020, 2020.